Hindawi
Shock and Vibration
Volume 2018, Article ID 6014570, 32 pages
https://doi.org/10.1155/2018/6014570

Research Article

Influence of the Eccentric Error of Star Gear on the Bifurcation Properties of Herringbone Star Gear Transmission with Floating Sun Gear

Fang Guo[1], **Zongde Fang**[1], **Xijin Zhang**[1] and **Yanmei Cui**[2]

[1] *School of Mechanical Engineering, Northwestern Polytechnical University, 127 West Youyi Road, Xi'an, Shaanxi 710072, China*
[2] *School of Mechatronics Engineering, Zhengzhou Institution of Aeronautical Industry Management, 2 Daxue Middle Street, Zhengzhou, Henan 450015, China*

Correspondence should be addressed to Zongde Fang; fauto@nwpu.edu.cn

Received 27 June 2017; Revised 19 November 2017; Accepted 3 December 2017; Published 16 January 2018

Academic Editor: Francesco Pellicano

Copyright © 2018 Fang Guo et al. This is an open access article distributed under the Creative Commons Attribution License, which permits unrestricted use, distribution, and reproduction in any medium, provided the original work is properly cited.

Taking a herringbone star gear transmission (HSGT) with floating sun gear as an example, the system bifurcation characteristics with the changing of the eccentric error of star gear and the working frequencies are analyzed. For this analysis, a generalized dynamic model of HSGT considering the manufacturing eccentric errors, time-varying mesh stiffness, and load balancing mechanism is established and solved by numerical method. The floating process of sun gear is explained. In this paper, there are seven cases about the eccentric errors of star gears which are calculated, respectively. To study the effect of the working frequencies (including meshing frequency and rotation frequency), the calculation is done at three kinds of input speed in which the working frequencies are close to the system natural frequencies. The results are demonstrated in detail by the bifurcation diagrams, phase plane plots, and Poincare maps. The system bifurcation characteristics are particularly analyzed and compared in every case. This work provides important guidance to the engineering of HSGT.

1. Introduction

Star gear transmission (SGT) is a power split transmission with fixed axis gears. This transmission uses star gears to load together, which form power branches. Unlike planetary gear train (PGT), the carrier of SGT is not rotating, and star gears only rotate on their axes. This difference results in no centrifugal force influencing on star gears when the SGT rotating in high speed and star gears can be lubricated continually, which benefits the smooth running of SGT [1]. In the decelerator of aeroengine and helicopter, it is broadly used due to its advantages such as compact dimension, low weight, and high load capability. However, manufacturing errors are inevitable when SGT is produced in a project, which must affect directly the dynamic response and load share capacity of SGT. Furthermore, the dynamic performance of SGT relates to the reliability and stability of the machinery which uses SGT. To resolve this problem, the load balance mechanism is widely adopted in SGT from home and abroad [2–4]. This method can improve the load sharing capability of SGT to some extent, but the dynamic properties of SGT will be must influenced. So, the study about the effect of manufacturing errors on the dynamic performance of SGT with load balance mechanism has a high value of practical application.

Many scholars have done a lot of research work about dynamic analysis of PGT. Most of them focus on dynamic behavior and load sharing of PGT [5–12]. The methods used by these research are classified into three main types: numerical analysis [10], finite element method [13, 14], and experiment [11]. The influence factors considered in the works consist mainly of meshing stiffness [15], support stiffness [16], assembly error, eccentric error [3, 11, 12, 17–19], profile modification [9], floating component [5, 17, 20], flexible component [21, 22], and so on.

However, the study with regard to SGT is rare so far. Sun et al. [23, 24] established a torsional and translational nonlinear dynamic model for SGT to predict the dynamic

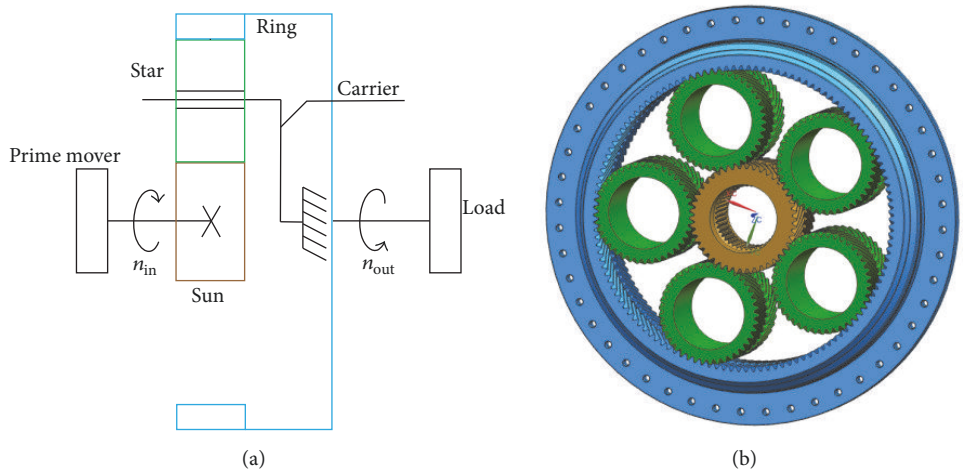

Figure 1: Herringbone star gear transmission. (a) Sketch map. (b) 3D model.

characteristics. They also use the Gill numerical method to obtain the dynamic response for a torsional nonlinear dynamic model of SGT and analyze the numerical results in time histories, phase plane plots, Poincare maps, and Fourier spectra. Bao and Zhu [25] develop a dynamic analysis model for a two-stage star gear train considering manufacturing and assembly errors to analyze the characteristics of sharing load and some relations between errors and the load sharing coefficient. Mo et al. [1, 26] probe into the natural characteristics and load sharing behavior of double-helical star gearing system for geared turbofan engine. Up to now, there are no literatures including the reports on the bifurcation and chaos of SGT with the manufacturing errors and load balance mechanism yet.

In this paper, using the lumped-parameter method and taking into account the manufacturing eccentric errors, time-varying mesh stiffness, and load balancing mechanism, a generalized dynamic model of HSGT with floating sun gear is presented to study the forced vibration characteristics. Sun gear is bore by a spline shaft with radial clearance, so it can float along the radial direction to improve unbalanced load which star gears bear because of eccentric errors. The evolution of system dynamic response is studied with changing eccentric errors of star gears which are divided into seven cases, and the process from periodic motions to chaos is shown by bifurcation diagrams, phase plane plots, and Poincare maps. The effect of the variation of working frequencies is also investigated by choosing three kinds of working speed in which the working frequencies are close to the system natural frequencies.

2. Dynamic Model of HSGT with Floating Sun Gear

Figure 1 depicts the structure of HSGT. It includes a sun gear, N star gears (N, the number of star gears), a ring gear, and a carrier. The input power is transmitted by sun gear and distributed by N star gears which form power branches, confluent in ring gear finally.

In order to build the dynamic model of HSGT, the following principles of treatment are adopted. In the case of engaging correctly, the axial forces exerted by left handed helical angle and right handed helical angle of herringbone gear are counteractive. Based on this feature of herringbone gear, the axial motion of gear is not considered, and only the radial and torsional motions of gear need to be taken into account. The carrier has radial two degrees of freedom (axial and torsional support stiffness is deemed very high). Gears are treated as rigid discs. Gear meshing is treated as a spring which has time-varying stiffness and acts on the gear tooth surface along the meshing line direction. The support from bearings and shaft to sun gear, the ring, and the carrier is equivalent to spring fastened to the foundation. The support from the carrier, bearings, and shaft to star gears is equivalent to the stiffness of carrier and shaft and the stiffness of bearings calculated by cascade spring connection calculation method. Star gears are assumed to be equispaced and same in mass, moment of inertia, support stiffness, and so on. The effect of friction is not taken into account. Based on these principles, the lumped-parameter dynamic model is constructed, as shown in Figure 2.

The indexing conventions s, r, and c for sun gear, ring gear, and the carrier, pi or p for star gears, $i = 1, 2, \ldots, N$ for the sequence number of star gears, spi for ith sun-star meshing pair, and pir for ith star-ring meshing pair are maintained throughout this paper.

As shown in Figure 2, the coordinate systems are built as follows: $o_j x_j y_j$ $(j = s, r, c, pi)$ is a fixed coordinate system, and its coordinate origin o_j $(j = s, r, c, pi)$ is located in the center of mass for the components. The indexing conventions K_{jx}, K_{jy} and C_{jx}, C_{jy} $(j = s, r, c, p)$ denote the support stiffness and support damping in x and y separately. K_{spi}, K_{pir} and C_{spi}, C_{pir} are the time-varying mesh stiffness and mesh damping separately, and e_{spi}, e_{pir} stand for the transmission error along the end meshing line direction.

The model has $8 + N \times 3$ degrees of freedom, and its generalized coordinates are as follows: $[x_s, y_s, u_s, x_r, y_r, u_r, x_c, y_c, x_{pi}, y_{pi}, u_{pi}]$, where x_j, y_j $(j = s, r, c, pi)$ are the translational displacement along x-axis and y-axis, u_j $(j = s, r, pi)$ is the rotational displacement around the z-axis, with $u_j = \theta_j \cdot r_{bj}$,

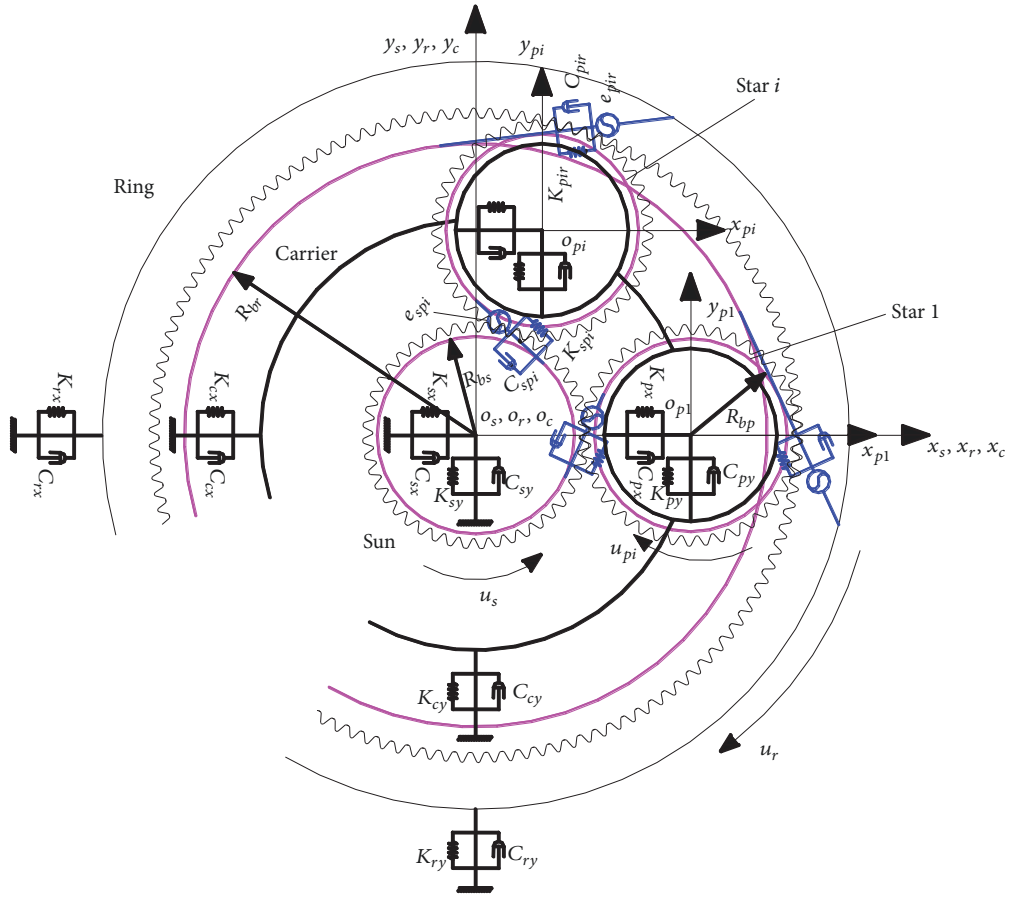

Figure 2: Dynamic model of herringbone star gear transmission.

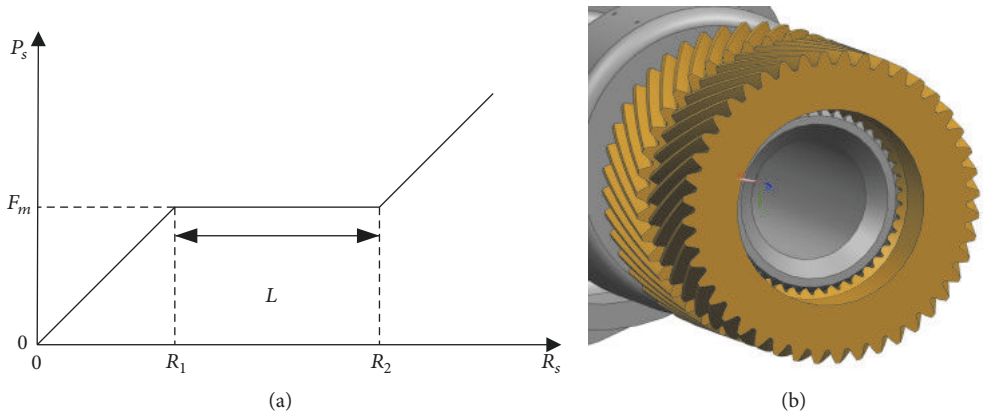

Figure 3: (a) Sketch map of the support reaction force. (b) 3D model of the spline support structure.

θ_j $(j = s, r, pi)$ is the angular displacement around z-axis, and r_{bj} $(j = s, r, p)$ are the radii of base circles.

3. Analysis of Floating Process of Sun Gear and Internal Excitation

3.1. Analysis of Floating Process of Sun Gear. The power is transmitted to sun gear by the spline shaft. Because of radial clearance existing between the inner and outer spline, when sun gear bears unbalance force, it can float in radial direction until the force becomes balanced.

In Figure 3, the sketch map expresses the support reaction force which sun gear bears. The horizontal axis denotes the floating amount of sun gear R_s, with $R_s = \sqrt{x_s^2 + y_s^2}$. The vertical axis denotes the support reaction force of the spline shaft P_s. F_m is the friction between the inner and outer spline,

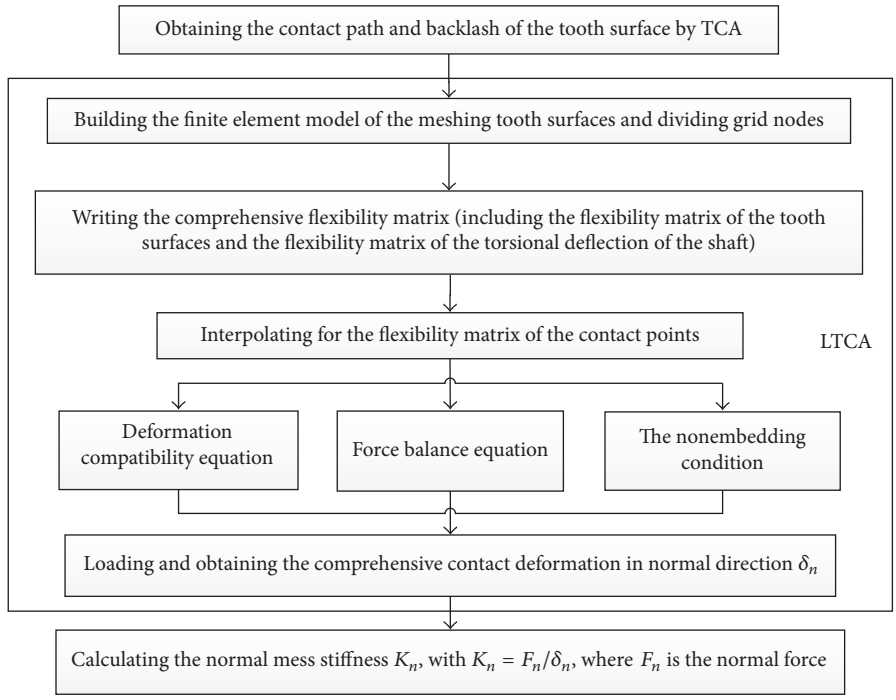

Figure 4: The procedure of the time-varying mesh stiffness.

with $F_m = \tau \cdot F_n$, where τ is the friction coefficient, F_n is the normal pressure which the tooth surface of the spline sustains. L is the radial clearance between the inner and outer spline, with $L = R_2 - R_1$.

As can be seen from Figure 3, in the floating process, sun gear bears mesh forces of N star gears and the support reaction force of the spline shaft. If $P_s \le F_m$, the slipping does not happen between the inner and outer spline. The stiffness of the spline shaft can be reduced on the premise of meeting the requirement of intensity, so the bending deformation of the spline shaft will fit the radial displacement of sun gear. At the moment, the range of R_s is between 0 and R_1. If $P_s > F_m$, the inner and outer spline will show relative sliding, which fits the radial displacement of sun gear. At this stage, the range of R_s is between R_1 and R_2. However, when the radial clearance between the inner and outer spline disappears, the bending deformation of the spline shaft fits the radial displacement of sun gear again, and the range of R_s is greater than R_2. Based on the above analysis, the support reaction forces of the spline shaft along x-axis and y-axis are, respectively, defined as follows.

The support reaction force of the spline shaft along x-axis is as follows:

$$P_{sx} = \begin{cases} K_{sx} \cdot x_s + C_{sx} \cdot \dot{x}_s & 0 \le R_s \le R_1 \text{ or } R_s > R_2 \\ F_m \cdot \cos\psi & R_1 < R_s \le R_2. \end{cases} \quad (1)$$

The support reaction force of the spline shaft along y-axis is as follows:

$$P_{sy} = \begin{cases} K_{sy} \cdot y_s + C_{sy} \cdot \dot{y}_s & 0 \le R_s \le R_1 \text{ or } R_s > R_2 \\ F_m \cdot \sin\psi & R_1 < R_s \le R_2, \end{cases} \quad (2)$$

where ψ is the direction angle of the deformation vector (x_s, y_s).

3.2. Time-Varying Mesh Stiffness Excitation. In this paper, the time-varying mesh stiffness is computed by using tooth contact analysis (TCA) [27] and loaded tooth contact analysis (LTCA) [28]. The particular calculate process is shown in Figure 4. The object is the inner or outer meshed gears. TCA and LTCA are applied to obtain the comprehensive contact deformations δ_n in normal direction at n contact points of tooth surface in a meshing period (the so-called comprehensive contact deformation considers the effect of other teeth meshing simultaneously). Then, the normal force F_n which the contact tooth surfaces bear is calculated by the following formula:

$$F_n = F_t \cdot \cos\beta_b, \quad (3)$$

where β_b is the base helix angle and F_t is the tangent force, with

$$F_t = \frac{T_{\text{in}}}{N \cdot r_{bs}}, \quad (4)$$

where T_{in} is the input torque, N is the number of star gears, and r_{bs} is the radius of base circle of sun gear. The ratio of F_n and δ_n is the normal mess stiffness K_n at n contact points of tooth surface in a meshing period. Finally, the discrete values K_n need to be interpolated by piecewise cubic-Hermite's interpolation function and expressed as the periodic function in the form of 10-order Fourier series. According to the process above, a MATLAB program is wrote to solve the time-varying mesh stiffness. Using this program,

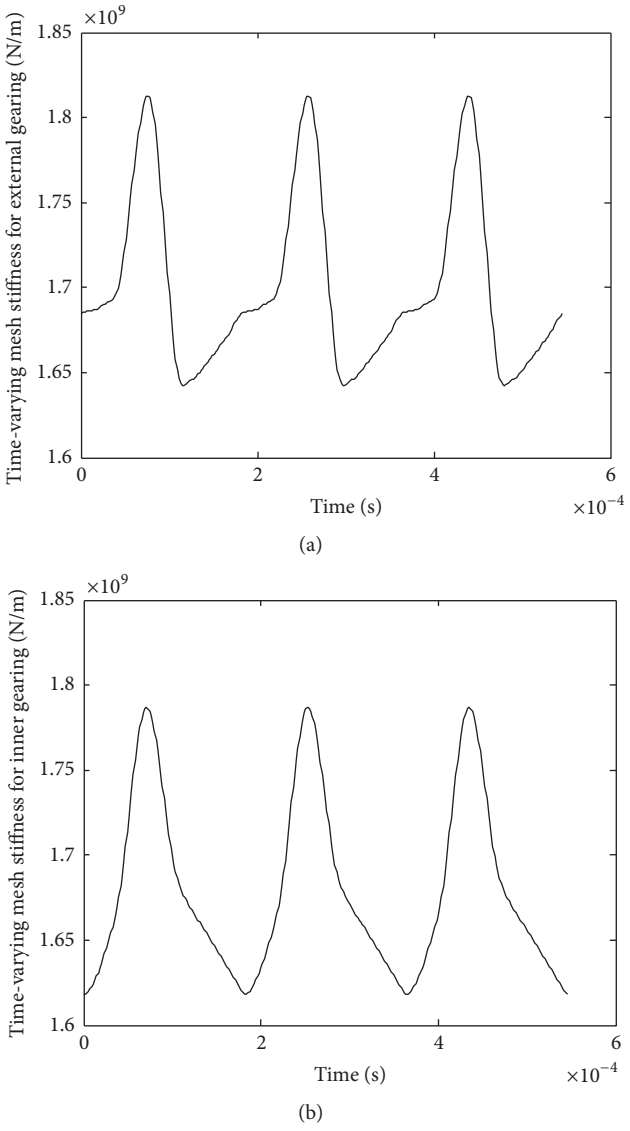

FIGURE 5: The time-varying mesh stiffness for external and inner gearing.

under various operating conditions, the time-varying mesh stiffness of gear pairs of various parameters can be calculated fast and efficiently. The mesh stiffness of the example in this paper is calculated, shown in Figure 5.

3.3. Eccentric Error Excitation. Figure 6 depicts the location relationships between the eccentric errors of sun gear and ith star gear and the end meshing line of ith sun-star pair. As shown here, the angle Φ_s between the eccentric error of sun gear E_s and the end meshing line of ith sun-star pair is

$$\Phi_s = \left(\frac{\pi}{2} - \alpha_w\right) + \varphi_{pi} - \left(\omega_s \cdot t + \gamma_s\right), \tag{5}$$

where α_w is the transverse pressure angle of external gearing, $\varphi_{pi} = 2\pi\ (i-1)/N$ is the assembly position angle of ith star gear, ω_s is the angular velocity of sun gear, and γ_s is the initial phase of the eccentric error of sun gear relative to x_s-axis. So

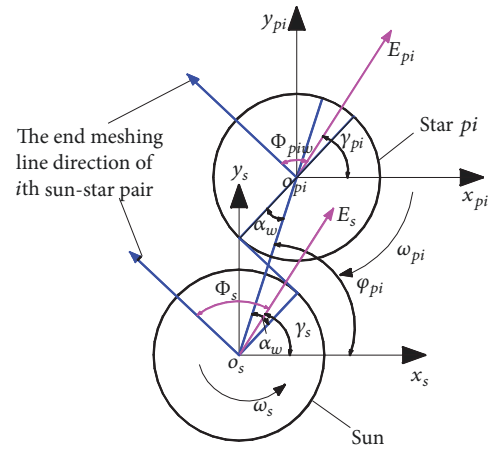

FIGURE 6: The location relationships of between the eccentric errors of sun gear and ith star gear and the end meshing line of ith sun-star pair.

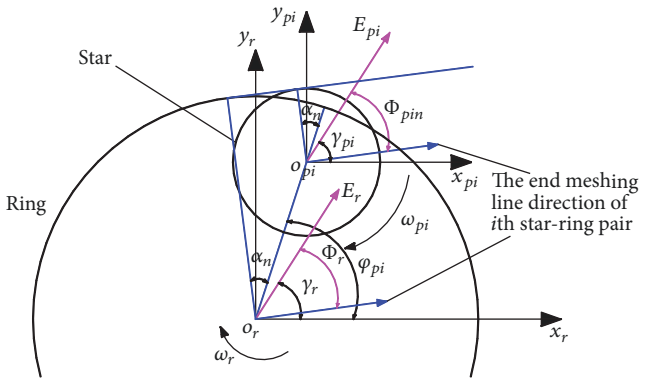

FIGURE 7: The location relationships of between the eccentric errors of ith star gear and ring gear and the end meshing line of ith star-ring pair.

the equivalent error of E_s projected to the end meshing line of ith sun-star pair is

$$\widetilde{E}_s = E_s \cdot \cos\Phi_s = E_s \cdot \sin\left(\omega_s \cdot t + \gamma_s + \alpha_w - \varphi_{pi}\right). \tag{6}$$

The angle Φ_{piw} between the eccentric error of star gear E_{pi} and the end meshing line of ith sun-star pair is

$$\Phi_{piw} = \left(\frac{\pi}{2} - \alpha_w\right) + \varphi_{pi} - \left(\omega_{pi} \cdot t + \gamma_{pi}\right), \tag{7}$$

where ω_{pi} is the angular velocity of star gear and γ_{pi} is the initial phase of the eccentric error of ith star gear relative to x_{pi}-axis. So the equivalent error of E_{pi} projected to the end meshing line of ith sun-star pair is

$$\begin{aligned}\widetilde{E}_{piw} &= E_{pi} \cdot \cos\Phi_{piw} \\ &= E_{pi} \cdot \sin\left(\omega_{pi} \cdot t + \gamma_{pi} + \alpha_w - \varphi_{pi}\right).\end{aligned} \tag{8}$$

Figure 7 depicts the location relationships of between the eccentric errors of ith star gear and ring gear and the end

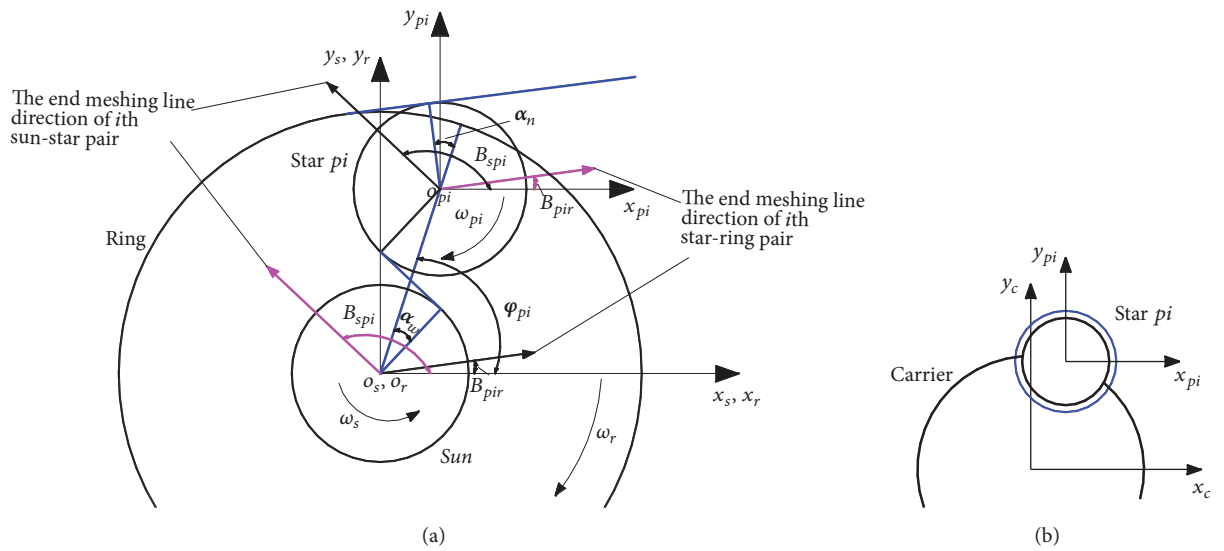

FIGURE 8: (a) The location relationships of between the displacement of the center of mass for gears and the end meshing line of ith sun-star and ith star-ring pair. (b) The location relationship of between the displacement of the center of mass for ith star gear and the carrier.

meshing line of ith star-ring pair. The angle Φ_{pin} between the eccentric error of the star E_{pi} and the end meshing line of ith star-ring pair is

$$\Phi_{pin} = \left(\frac{\pi}{2} - \alpha_n\right) + \left(\omega_{pi} \cdot t + \gamma_{pi}\right) - \varphi_{pi}, \tag{9}$$

where α_n is the transverse pressure angle of internal gearing. So the equivalent error of E_{pi} projected to the end meshing line of ith star-ring pair is

$$\begin{aligned}\widetilde{E}_{pin} &= E_{pi} \cdot \cos \Phi_{pin} \\ &= -E_{pi} \cdot \sin\left(\omega_{pi} \cdot t + \gamma_{pi} - \alpha_n - \varphi_{pi}\right).\end{aligned} \tag{10}$$

The angle Φ_r between the eccentric error of ring gear E_r and the end meshing line of ith star-ring pair is

$$\Phi_r = \left(\frac{\pi}{2} - \alpha_n\right) + \left(\omega_r \cdot t + \gamma_r\right) - \varphi_{pi}, \tag{11}$$

where ω_r is the angular velocity of ring gear and γ_r is the initial phase of the eccentric error of ring gear relative to x_r-axis. So the equivalent error of E_r projected to the end meshing line of ith star-ring pair is

$$\widetilde{E}_r = E_r \cdot \cos \Phi_r = -E_r \cdot \sin\left(\omega_r \cdot t + \gamma_r - \alpha_n - \varphi_{pi}\right). \tag{12}$$

Based on the above analysis, the equivalent displacements of the eccentric errors of gears are

$$\begin{aligned}e_{spi} &= \widetilde{E}_s + \widetilde{E}_{piw} \\ &= E_s \cdot \sin\left(\omega_s \cdot t + \gamma_s + \alpha_w - \varphi_{pi}\right) + E_{pi} \\ &\quad \cdot \sin\left(\omega_{pi} \cdot t + \gamma_{pi} + \alpha_w - \varphi_{pi}\right),\end{aligned}$$

$$\begin{aligned}e_{pir} &= \widetilde{E}_{pin} + \widetilde{E}_r \\ &= -E_{pi} \cdot \sin\left(\omega_{pi} \cdot t + \gamma_{pi} - \alpha_n - \varphi_{pi}\right) - E_r \\ &\quad \cdot \sin\left(\omega_r \cdot t + \gamma_r - \alpha_n - \varphi_{pi}\right),\end{aligned} \tag{13}$$

where e_{spi}, e_{pir} are, respectively, the equivalent errors for the ith sun-star pair and ith star-ring pair.

4. Motion Differential Equation of HSGT with Floating Sun Gear

According to the location relationships of between the displacement of the center of mass for gears and the end meshing line of ith sun-star pair and ith star-ring pair, as shown in Figure 8(a), the relative displacements of the translational gear pairs along the meshing line of ith sun-star pair and ith star-ring pair are separately defined as follows. The relative displacement of the translational gear pairs along the meshing line of ith sun-star pair are

$$\begin{aligned}\delta_{spi} &= \left[\left(x_s \cdot \cos B_{spi} + y_s \cdot \sin B_{spi} + u_s\right)\right. \\ &\quad \left. - \left(x_{pi} \cdot \cos B_{spi} + y_{pi} \cdot \sin B_{spi} + u_{pi}\right) + e_{spi}\right] \\ &\quad \cdot \cos \beta_b,\end{aligned} \tag{14}$$

where B_{spi} is the angle of the end meshing line of ith sun-star pair relative to x-axis, with $B_{spi} = \pi/2 - \alpha_w + \varphi_{pi}$. The relative displacement of the translational gear pair along the meshing line of ith star-ring pair is

$$\begin{aligned}\delta_{pir} &= \left[\left(x_{pi} \cdot \cos B_{pir} + y_{pi} \cdot \sin B_{pir} + u_{pi}\right)\right. \\ &\quad \left. - \left(x_r \cdot \cos B_{pir} + y_r \cdot \sin B_{pir} + u_r\right) + e_{pir}\right] \cdot \cos \beta_b,\end{aligned} \tag{15}$$

where B_{pir} is the angle of the end meshing line of ith star-ring pair relative to x-axis, with $B_{pir} = \varphi_{pi} - (\pi/2 - \alpha_n)$.

In Figure 8(b), the radial displacements of ith star gear relative to the carrier along x-axis and y-axis are separately defined as follows:

$$\begin{aligned} \delta_{picx} &= x_{pi} - x_c, \\ \delta_{picy} &= y_{pi} - y_c. \end{aligned} \tag{16}$$

Based on Newton's second law and the above analysis, the motion differential equations of components are listed as shown in

$$\begin{aligned} &M_s \cdot \ddot{x}_s + P_{sx} \\ &\quad + \sum_{i=1}^{5} \left[\left(C_{spi} \cdot \dot{\delta}_{spi} + K_{spi} \cdot \delta_{spi} \right) \cdot \cos\beta_b \cdot \cos B_{spi} \right] \\ &\quad = 0, \\ &M_s \cdot \ddot{y}_s + P_{sy} \\ &\quad + \sum_{i=1}^{5} \left[\left(C_{spi} \cdot \dot{\delta}_{spi} + K_{spi} \cdot \delta_{spi} \right) \cdot \cos\beta_b \cdot \sin B_{spi} \right] \\ &\quad = 0, \\ &\frac{I_s}{r_{bs}^2} \cdot \ddot{u}_s + \sum_{i=1}^{5} \left(C_{spi} \cdot \dot{\delta}_{spi} + K_{spi} \cdot \delta_{spi} \right) \cdot \cos\beta_b = \frac{T_{\text{in}}}{r_{bs}}, \end{aligned} \tag{17a}$$

$$\begin{aligned} &M_p \cdot \ddot{x}_{pi} + C_{px} \cdot \dot{\delta}_{picx} + K_{px} \cdot \delta_{picx} \\ &\quad - \left[\left(C_{spi} \cdot \dot{\delta}_{spi} + K_{spi} \cdot \delta_{spi} \right) \cdot \cos\beta_b \cdot \cos B_{spi} \right] \\ &\quad + \left[\left(C_{pir} \cdot \dot{\delta}_{pir} + K_{pir} \cdot \delta_{pir} \right) \cdot \cos\beta_b \cdot \cos B_{pir} \right] \\ &\quad = 0, \\ &M_p \cdot \ddot{y}_{pi} + C_{py} \cdot \dot{\delta}_{picy} + K_{py} \cdot \delta_{picy} \\ &\quad - \left[\left(C_{spi} \cdot \dot{\delta}_{spi} + K_{spi} \cdot \delta_{spi} \right) \cdot \cos\beta_b \cdot \sin B_{spi} \right] \\ &\quad + \left[\left(C_{pir} \cdot \dot{\delta}_{pir} + K_{pir} \cdot \delta_{pir} \right) \cdot \cos\beta_b \cdot \sin B_{pir} \right] = 0, \\ &\frac{I_p}{r_{bp}^2} \cdot \ddot{u}_{pi} - \left(C_{spi} \cdot \dot{\delta}_{spi} + K_{spi} \cdot \delta_{spi} \right) \cdot \cos\beta_b \\ &\quad + \left(C_{pir} \cdot \dot{\delta}_{pir} + K_{pir} \cdot \delta_{pir} \right) \cdot \cos\beta_b = 0, \end{aligned} \tag{17b}$$

$$\begin{aligned} &M_c \cdot \ddot{x}_c + C_{cx} \cdot \dot{x}_c + K_{cx} \cdot x_c \\ &\quad - \sum_{i=1}^{5} \left(C_{px} \cdot \dot{\delta}_{picx} + K_{px} \cdot \delta_{picx} \right) = 0, \\ &M_c \cdot \ddot{y}_c + C_{cy} \cdot \dot{y}_c + K_{cy} \cdot y_c \\ &\quad - \sum_{i=1}^{5} \left(C_{py} \cdot \dot{\delta}_{picy} + K_{py} \cdot \delta_{picy} \right) = 0, \end{aligned} \tag{17c}$$

$$\begin{aligned} &M_r \cdot \ddot{x}_r + C_{rx} \cdot \dot{x}_r + K_{rx} \cdot x_r \\ &\quad - \sum_{i=1}^{5} \left[\left(C_{pir} \cdot \dot{\delta}_{pir} + K_{pir} \cdot \delta_{pir} \right) \cdot \cos\beta_b \cdot \cos B_{pir} \right] \\ &\quad = 0, \\ &M_r \cdot \ddot{y}_r + C_{ry} \cdot \dot{y}_r + K_{ry} \cdot y_r \\ &\quad - \sum_{i=1}^{5} \left[\left(C_{pir} \cdot \dot{\delta}_{pir} + K_{pir} \cdot \delta_{pir} \right) \cdot \cos\beta_b \cdot \sin B_{pir} \right] \\ &\quad = 0, \\ &\frac{I_r}{r_{br}^2} \cdot \ddot{u}_r - \sum_{i=1}^{5} \left(C_{pir} \cdot \dot{\delta}_{pir} + K_{pir} \cdot \delta_{pir} \right) \cdot \cos\beta_b \\ &\quad = -\frac{T_{\text{out}}}{r_{br}}, \end{aligned} \tag{17d}$$

where M_j ($j = s, p, r, c$) are the mass of each component, I_j ($j = s, p, r$) are the moment of inertia, P_{sx}, P_{sy} are depicted in (1) and (2), the support stiffness K_{jx}, K_{jy} ($j = s, p, r, c$) are abstained by FEA, and the support damping C_{jx}, C_{jy} ($j = s, p, r, c$) are calculated by using this formula, which is

$$\begin{aligned} C_{jx} &= 2\xi_t \sqrt{K_{jx} M_j}, \\ C_{jy} &= 2\xi_t \sqrt{K_{jy} M_j} \end{aligned} \tag{18}$$

(see [1]), where ξ_t is the support damping ratio, whose value is 0.003 in this paper. C_{spi}, C_{pir} are the mesh damping coefficient of engagement pairs, with

$$\begin{aligned} C_{spi} &= 2\xi \sqrt{\frac{\overline{K}_{spi} I_s I_p}{I_s r_{bp}^2 + I_p r_{bs}^2}}, \\ C_{pir} &= 2\xi \sqrt{\frac{\overline{K}_{pir} I_p I_r}{I_p r_{br}^2 + I_r r_{bp}^2}}, \end{aligned} \tag{19}$$

where ξ is mesh damping ratio, whose value is 0.03 in this paper. $\overline{K}_{spi}$, $\overline{K}_{pir}$ are the mean mesh stiffness of each engagement pair, and T_{in}, T_{out} are, respectively, input torque and load torque.

5. Simulation and Analysis

A herringbone star gear transmission (HSGT) with floating sun gear and five equally spaced star gears ($N = 5$) is used as an example, and the motion differential equation is solved by Runge-Kutta numerical calculation method. The parameters of the example are shown in Table 1.

In this chapter, the focus is the effect of eccentric errors of star gears with different phase and number on the dynamic response of HSGT with floating sun gear. So the eccentric errors of sun gear and ring gear are set to 0 μm. According to the place and number of star gears, the cases of star gears

Table 1: Parameters of the herringbone star gear transmission.

Parameters	Sun	Star	Carrier	Ring
Number of teeth, Z	44	41	-	126
Normal modulus, m_n (mm)	3.5	3.5	-	3.5
Normal pressure angle, α_n (deg.)	22.5	22.5	-	22.5
Helix angle, $\boldsymbol{\beta}$ (deg.)	28	28	-	28
Helical tooth width, b (mm)	60	60	-	55
Mass, M (kg)	68	11.3	83	207.7
Inertia, I (kg·m^2)	0.42	0.06	-	8.58
Support stiffness in x, y-direction (N/m)	$K_{sx,y} = 3.52 \times 10^7$	$K_{px,y} = 1.61 \times 10^9$	$K_{cx,y} = 2.56 \times 10^8$	$K_{rx,y} = 1.46 \times 10^8$
Mean meshing stiffness in the direction of contact line (N/m)	$\overline{K}_{spi} = 1.7 \times 10^9$		$\overline{K}_{pir} = 1.68 \times 10^9$	
The value of the radial clearance between inner and outer spline, L (μm)	50			
Input speed, n_s (r/min)	7500			
Input power, T_{in} (Kw)	1000			

Note. The mass and inertia of sun gear and ring gear include the mass and inertia of input and output shaft.

Table 2: The cases of star gears carrying eccentric error.

Cases	1	2	3	4	5	6	7
Sequence number of star gears	1	1, 2	1, 2, 3	1, 2, 3, 4	1, 2, 3, 4, 5	1, 3	1, 2, 4

carrying eccentric errors are divided into seven patterns, shown in Table 2.

Setting the initial phase of the eccentric error of star gear equal to its assembly position angle, changing the eccentric errors from 0 μm to 50 μm, we solve the system motion differential equation for the bifurcation behaviors. To study the regularity of the system motion development, the bifurcation diagrams on the relative vibration displacement between sun gear and star gear for the seven situations shown in Table 2 are given. Aiming at some typical system motion form, the phase plane plots, Poincare maps are given.

In the seven cases, there are about four kinds of motion appearing in the system. They are periodic, period-doubling, quasiperiod, and chaos motion. How to judge the three motions, towards periodic or period-doubling motion, the phase plane plot is a regular curve, the Poincare map of periodic motion is a dot, and the Poincare map of period-doubling motion is composed of dots which collect on several areas; to quasiperiod motion, the phase plane plot is a belt-like curve, and the Poincare map is composed of dots looking like serial; for chaos, the phase plane plot is a curve whose shape is noncircular and nonelliptic, and the Poincare map is composed of dots arranged disorderly. It is difficult to distinguish the quasiperiod motion and chaos in the bifurcation diagram, so the phase plane plots and Poincare maps are needed to comprehensively observe.

To study the effect of the variation of system working frequency on the dynamic characteristics of HSGT, we give the 23th order natural frequencies of HSGT in two situations of floating and nonfloating, shown in Table 3. At speed 4251.8 r/min, Cases 1, 5, and 6 are calculated. Under this speed, the meshing frequency is close to the 14th and 15th order natural frequencies. At speeds 5862 r/min and 7320 r/min, Case 1 is calculated. Under these two speeds, the rotation frequency is close to the second and third-order natural frequencies in the floating and nonfloating state, shown in Table 4.

5.1. The System Bifurcation Characteristics with Changing Eccentric Errors of Adjacent Star Gears

Case 1 (star gear 1 with eccentric error). The system dynamic response is shown in Figure 9. It can be seen from the enlarged images in Figure 9 that the system response bifurcates into period-doubling from single-periodic motion where $E_{p1} = 24\,\mu$m. When the eccentric error of star gear 1 is greater than 24 μm, the system motion bifurcates into complicated motion state (quasiperiod or chaos). The phase plane plots and Poincare maps of the system response where $E_{p1} = 24\,\mu$m are shown in Figure 10. As can be seen from Figures 10(b), 10(f), and 10(h) that there is period 5 motion appearing in the system, Figure 11 describes the phase plane plots and Poincare maps of the system response where $E_{p1} = 42\,\mu$m. In Figure 11(e), it is quite clear that chaos develops in the system. We can also conclude that the gear pairs of sun-star 2 and sun-star 5 have the same dynamic characteristics, so do the gear pairs of sun-star 3 and sun-star 4.

Case 2 (star gears 1 and 2 with eccentric errors). Figure 12 depicts the system bifurcation characteristic with the

Table 3: The natural frequencies of HSGT.

Ranks	Natural frequency (Hz)	
	Floating	Nonfloating
1	0	0
2, 3	97.7 (97.7)	122.0 (122.0)
4, 5	159.2 (159.2)	167.6 (167.6)
6	824.1	824.1
7, 8	946.8 (946.8)	948.5 (948.5)
9, 10	1699.2 (1699.2)	1699.2 (1699.2)
11	1749.0	1749.0
12, 13	2074.8 (2074.8)	2074.9 (2074.9)
14, 15	3118.0 (3118.0)	3118.0 (3118.0)
16, 17	3204.7 (3204.7)	3204.7 (3204.7)
18, 19	3252.8 (3252.8)	3252.8 (3252.8)
20	3280.4	3280.4
21, 22	3416.5 (3416.5)	3416.7 (3416.7)
23	3572.4	3572.4

Table 4: The working frequencies of HSGT at three speeds.

Input speed (r/min)	Working frequency (Hz)			
	Shaft frequency (Hz)			Meshing frequency (Hz)
	Sun	Star	Ring	
4251.8	70.9	76.0	24.6	**3118.0**
5862	**97.7**	104.8	34.1	4298.8
7320	**122.0**	130.9	42.6	5368.0

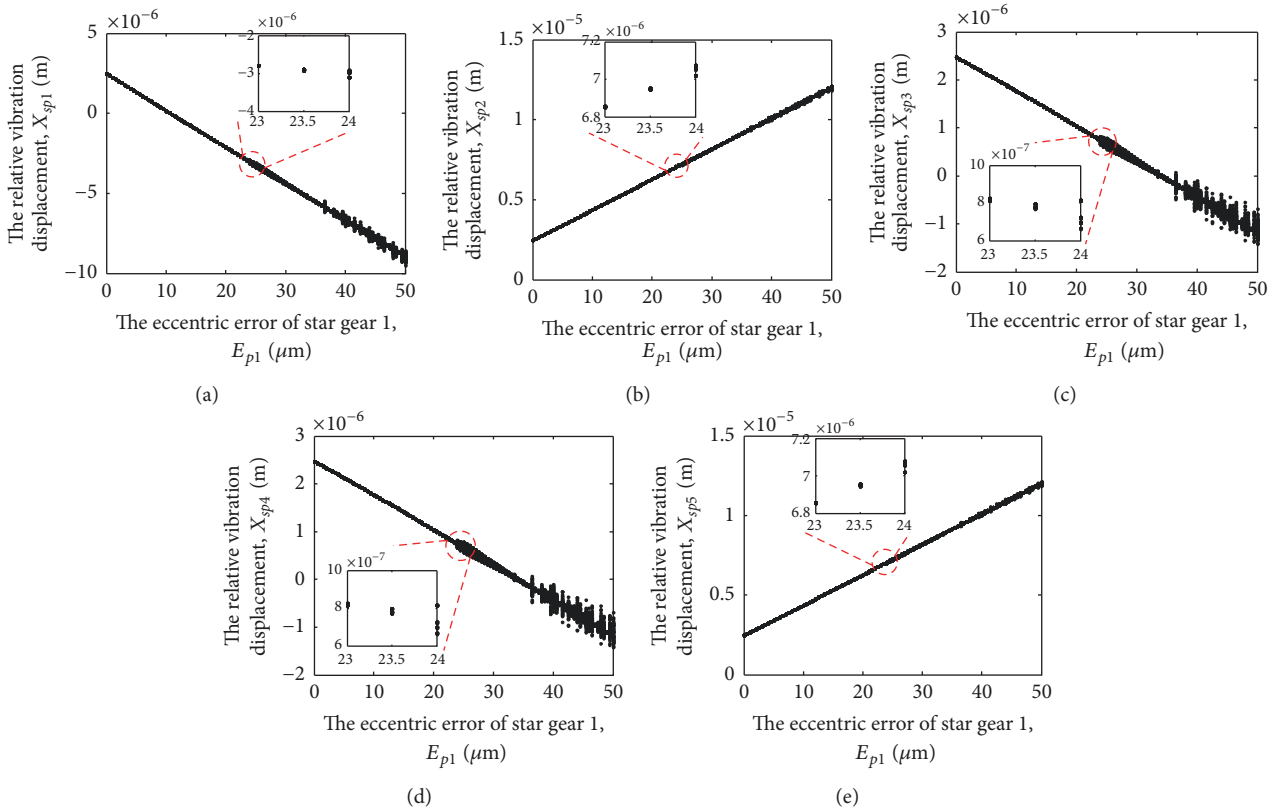

Figure 9: The system bifurcation diagram with the variation of eccentric error of star gear 1.

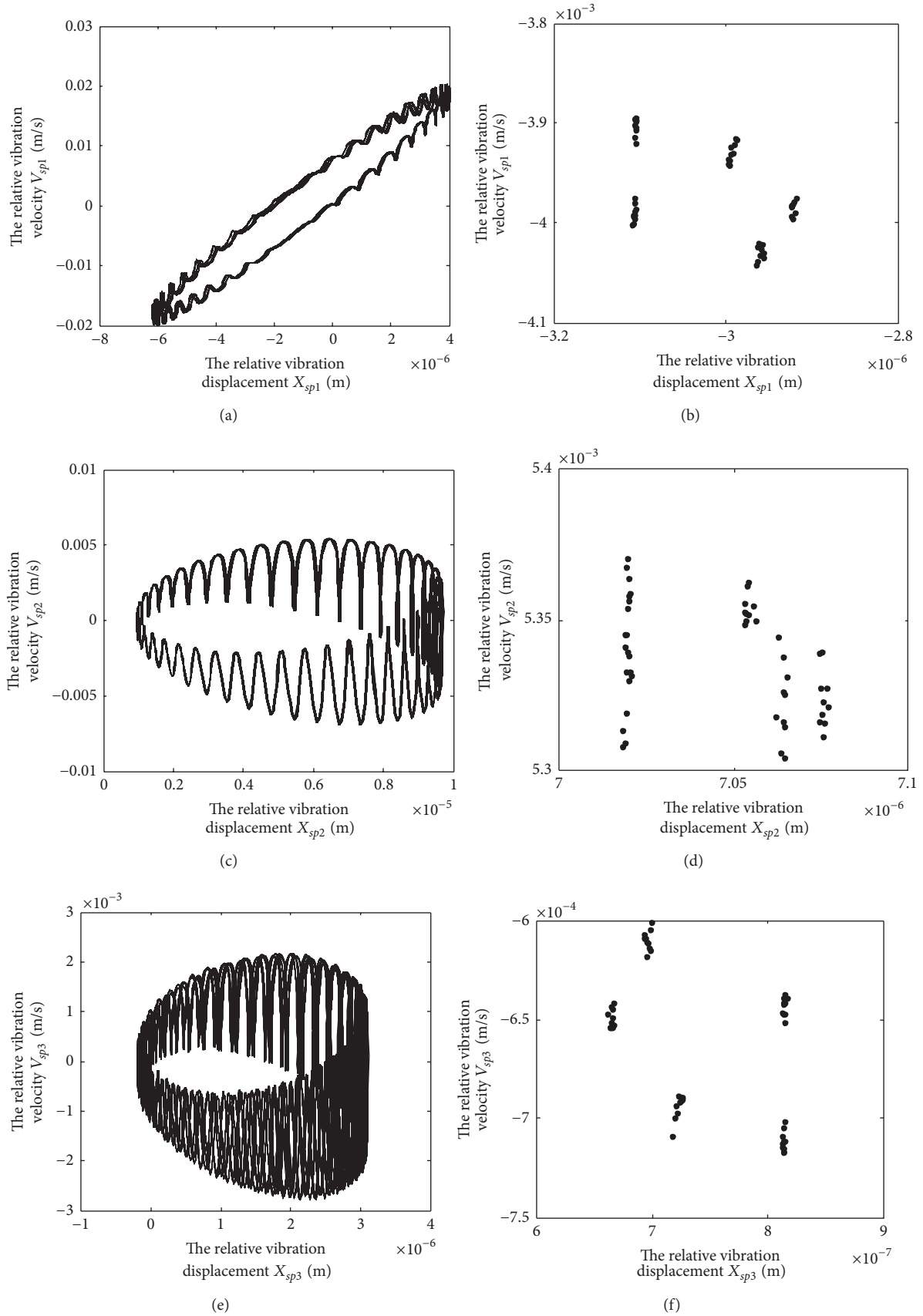

Figure 10: Continued.

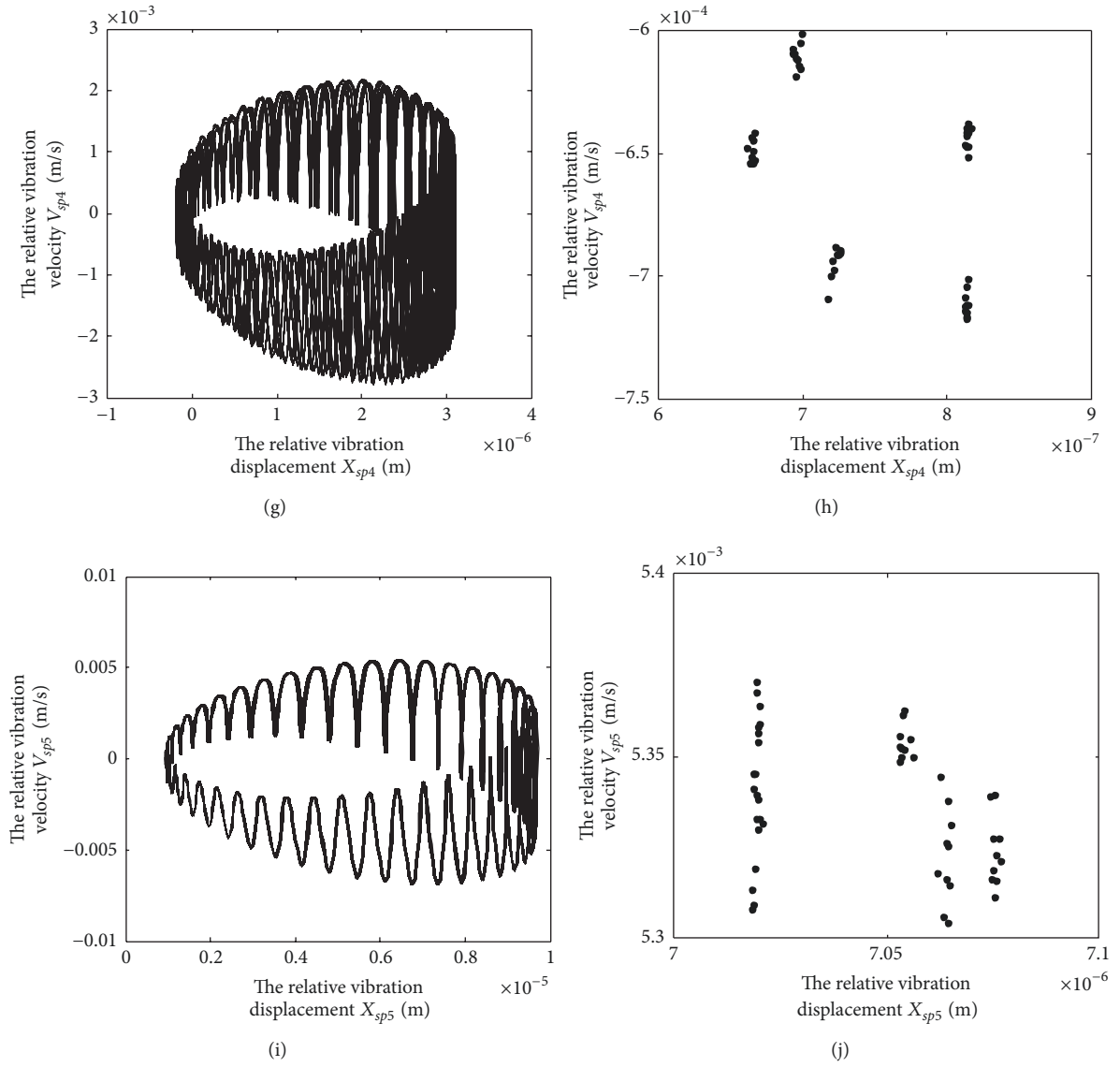

FIGURE 10: The phase plane plots and Poincare maps for five sun-star pairs, when $E_{p1} = 24\,\mu$m. (a), (c), (e), (g), and (i) are the phase plane plots. (b), (d), (f), (h), are (j) are the Poincare maps.

changing of eccentric errors of star gears 1 and 2. We can see that the gear pairs of sun-star 1 and sun-star 2 have the same dynamic characteristics, so do the gear pairs of sun-star 3 and sun-star 5. From Figures 9 and 12, it can be drawn that the effect of the eccentric errors of star gears 1 and 2 on the system response is greater than one of star gears 1. In Case 2, the system response bifurcates into period-doubling from periodic motion where $E_{p1,2} = 15\,\mu$m. Beginning around $E_{p1,2} = 20\,\mu$m, the system response shows the complex bifurcation characteristics. As shown in Figures 13 and 14, there are period 5 motion and chaos, respectively, appearing in the system where $E_{p1,2} = 15\,\mu$m and $22.5\,\mu$m. In Figures 14(a) and 14(e), the curves distort.

Case 3 (star gears 1, 2, and 3 with eccentric errors). It is the same as Case 2 that the system response bifurcates into period 5 from periodic motion where $E_{p1,2,3} = 15\,\mu$m and the two cases have the similar bifurcation characteristics shown in Figures 12 and 15. The difference from Case 2 is that the gear pairs of sun-star 1 and sun-star 3 have the same dynamic characteristics, so do the gear pairs of sun-star 4 and sun-star 5. Figures 16 and 17 separately depict the phase plane plots and Poincare maps between sun gear and five star gears, where $E_{p1,2,3} = 15\,\mu$m and $26.5\,\mu$m. There are period 5 and chaos motion, respectively, appearing in the system.

Case 4 (star gears 1, 2, 3, and 4 with eccentric errors). As shown in Figure 18, the system response is relatively stable compared with Cases 2 and 3, which bifurcates into period-doubling motion starting with $E_{p1,2,3,4} = 18.5\,\mu$m. Each sun-star pair has different dynamic characteristics. The sun-star 1 pair is the most stable in five sun-star pairs. Figures 19 and 20

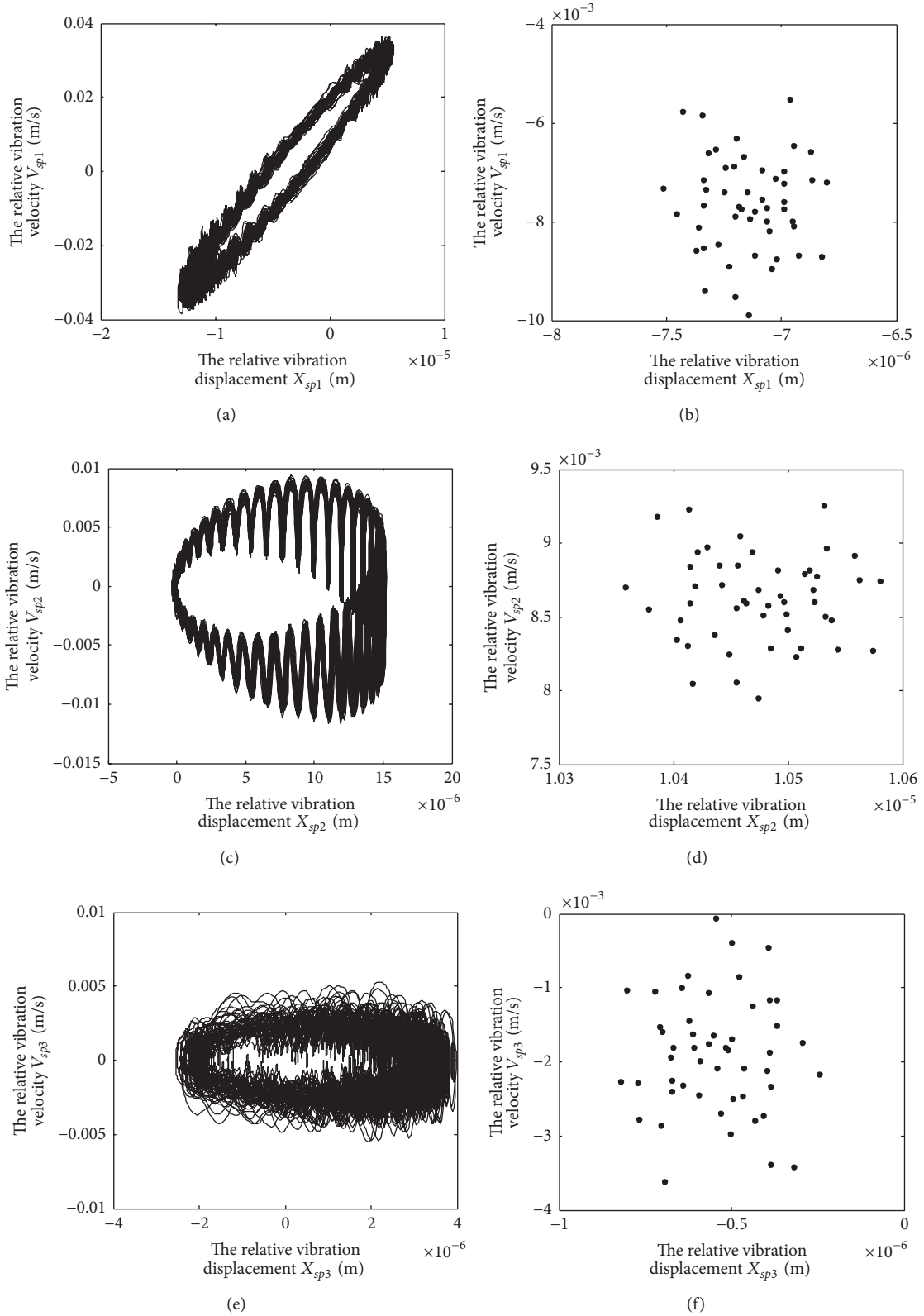

FIGURE 11: The phase plane plots and Poincare maps for five sun-star pairs, when $E_{p1} = 42\,\mu$m. (a), (c), and (e) are the phase plane plots. (b), (d), and (f) are the Poincare maps (note: only one of the gear pairs which have the same dynamic characteristics is shown).

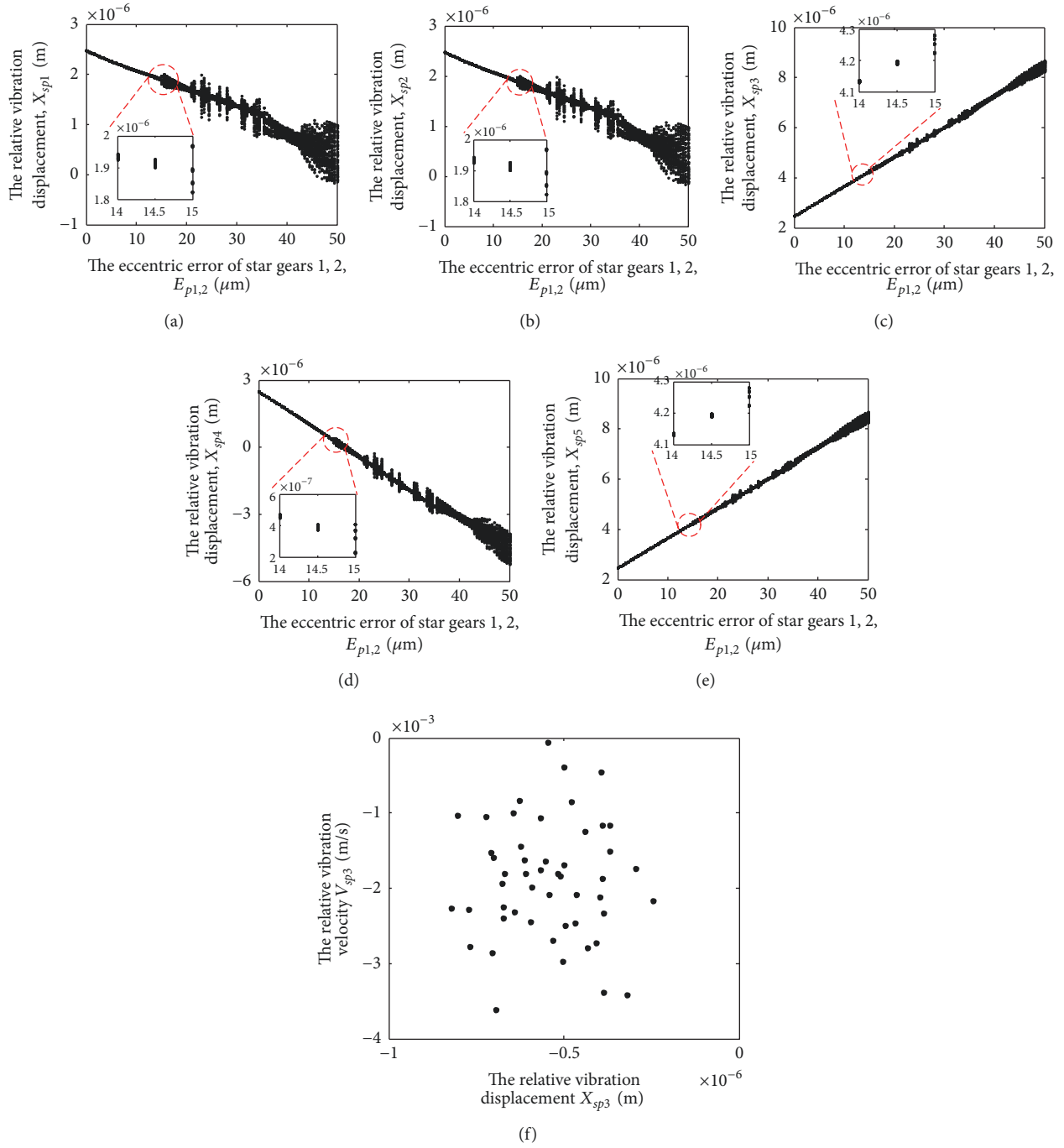

Figure 12: The system bifurcation diagram with the variation of eccentric error of star gears 1 and 2.

depict the phase plane plots and Poincare maps between sun gear and five star gears, where $E_{p1,2,3,4}$ = 18.5 μm and 44 μm. There are period 5 and chaos motion, respectively, appearing in the system.

Case 5 (star gears 1, 2, 3, 4, and 5 with eccentric errors). In the case, the system response is more stable than Case 4, which bifurcates into quasiperiod motion starting with $E_{p1,2,3,4,5}$ = 45 μm shown in Figure 21. From the figure, we can see that the gear pairs of sun-star 1 and sun-star 2 have the same dynamic characteristics, so do the gear pairs of sun-star 3 and sun-star 5. It is corresponding to discover that the system always keeps the quasiperiod motion by calculating the system response where $E_{p1,2,3,4,5}$ = 45 μm, 46 μm, 48 μm, and 50 μm. Figure 22 depicts the phase plane plots and Poincare maps between sun gear and five star gears, where $E_{p1,2,3,4,5}$ = 45 μm.

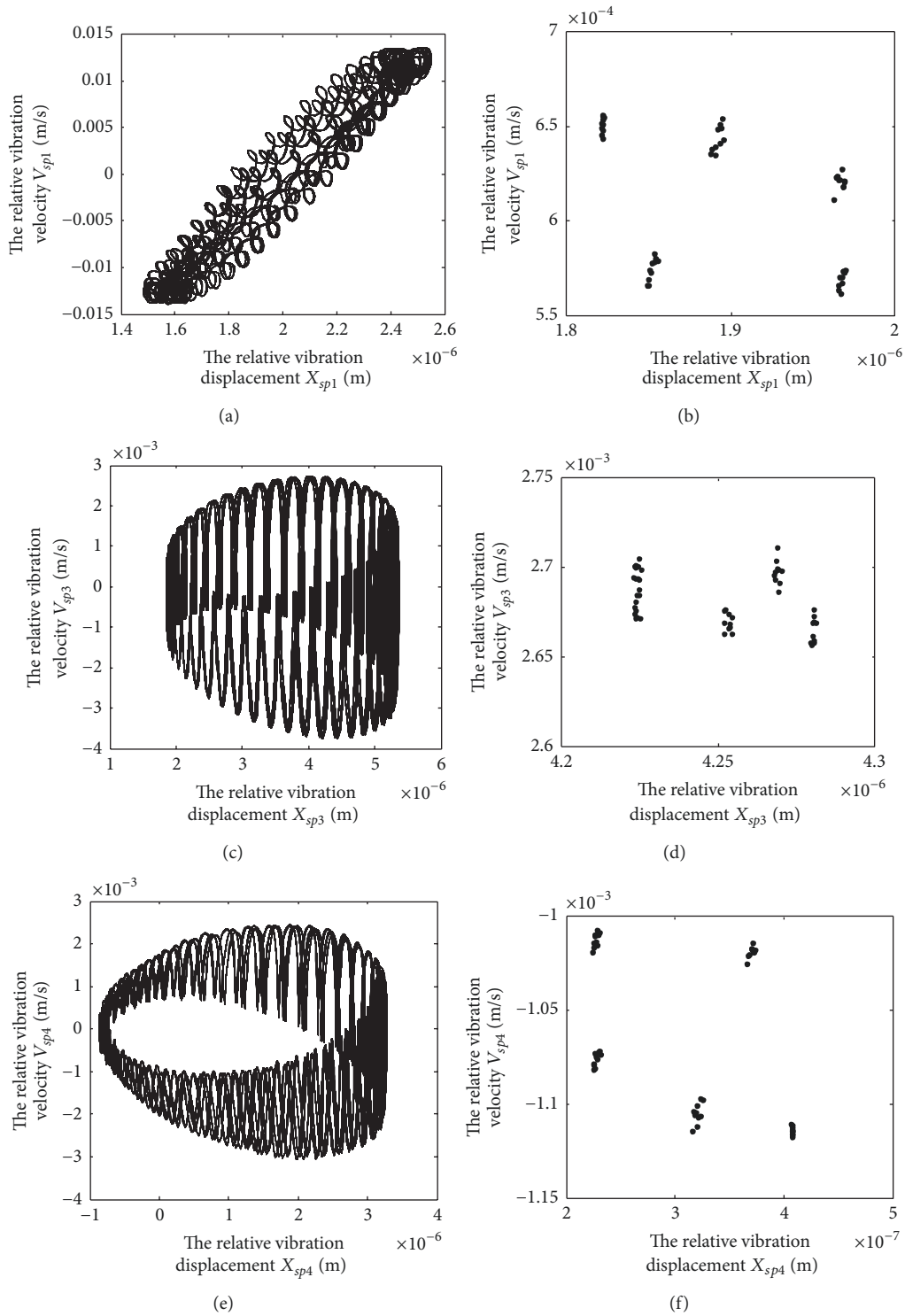

FIGURE 13: The phase plane plots and Poincare maps for five sun-star pairs, when $E_{p1,2} = 15\,\mu$m. (a), (c), and (e) are the phase plane plots. (b), (d), and (f) are the Poincare maps (note: only one of the gear pairs which have the same dynamic characteristics is shown).

5.2. The System Bifurcation Characteristics with Changing Eccentric Errors of Nonadjacent Star Gears

Case 6 (star gears 1 and 3 with eccentric errors). In this case, the influence of eccentric errors of star gears 1 and 3 on the system response is significantly less than one of star gears 1 and 2 in Case 2. The system motion bifurcates into period-doubling motion beginning with $E_{p1,3} = 39\,\mu$m shown in Figure 23. The gear pairs of sun-star 1 and sun-star 3 have the same dynamic characteristics, so do the gear pairs of sun-star

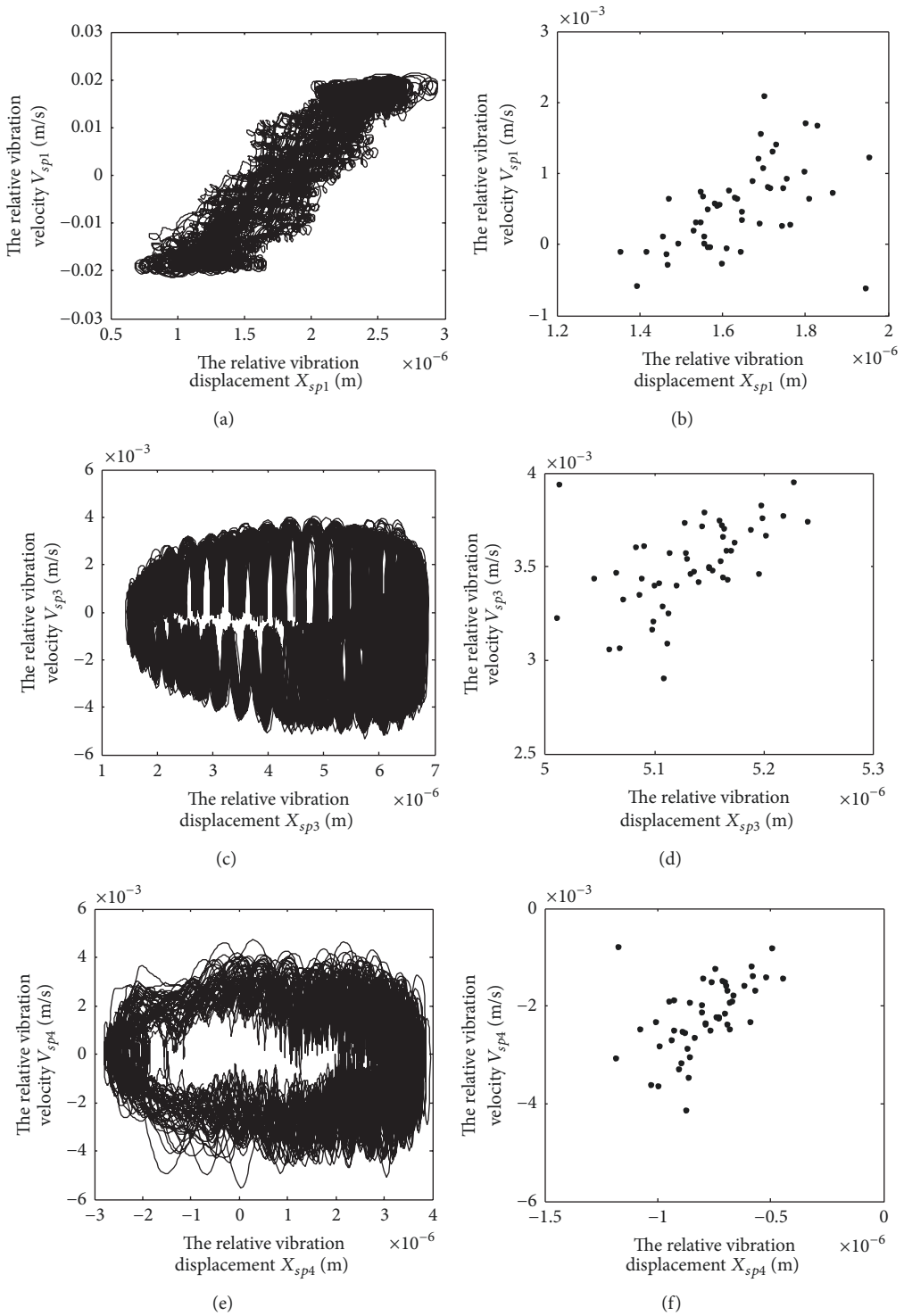

FIGURE 14: The phase plane plots and Poincare maps for five sun-star pairs, when $E_{p1,2} = 22.5\,\mu$m. (a), (c), and (e) are the phase plane plots. (b), (d), and (f) are the Poincare maps (note: only one of the gear pairs which have the same dynamic characteristics is shown).

4 and sun-star 5. Figure 24 describes the phase plane plots and Poincare maps between sun gear and five star gears where $E_{p1,3} = 39\,\mu$m. From Figure 24(f), it can be seen that period 5 motion develops in the system.

Case 7 (star gears 1, 2, and 4 with eccentric errors). In this case, the system response is obviously more stable than Case 3. The system motion bifurcates into quasiperiod motion beginning with $E_{p1,2,4} = 20.5\,\mu$m shown in Figure 25. The

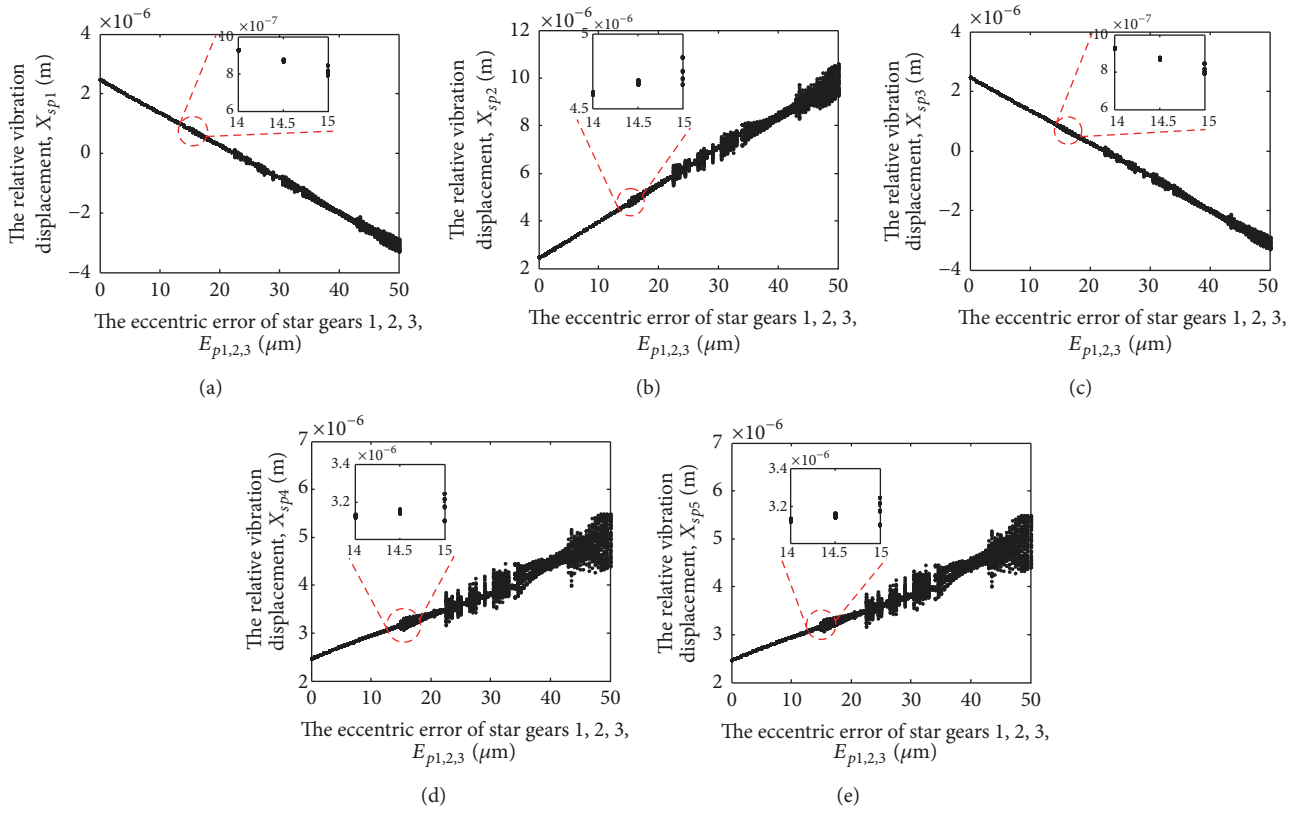

Figure 15: The system bifurcation diagram with the variation of eccentric error of star gears 1, 2, and 3.

Table 5: A comparison of the error values of beginning to bifurcate.

Input speed (r/min)	Error value (μm) Beginning to bifurcate		
	Case 1	Case 5	Case 6
4251.8	9.5	23.5	15.5
7500	24	44.5	20.5

gear pairs of sun-star 1 and sun-star 2 have the same dynamic characteristics, so do the gear pairs of sun-star 4 and sun-star 5. After about $E_{p1,2,4} = 34\,\mu$m, the system shows the complex bifurcation characteristics. Figures 26 and 27 describe the phase plane plots and Poincare maps between sun gear and five star gears where $E_{p1,2,4} = 20.5\,\mu$m and $37\,\mu$m. In Figure 27, there is the tendency of chaos motion appearing in the system.

5.3. The System Bifurcation Characteristics with the Working Frequencies Close to the Fundamental Natural Frequencies of the System

5.3.1. Calculating Cases 1, 5, and 6 at Speed 4251.8 r/min. When the input speed is 4251.8 r/min, the meshing frequency is equal to the 14th and 15th order natural frequencies shown in Tables 3 and 4. At this speed, we calculate Cases 1, 5, and 6 and plot the bifurcation diagrams shown in Figures 28, 29, and 30. Comparing with Figures 9, 21, and 23, we can see that the error values of beginning to bifurcate decrease in Cases 1 and 6 and the system shows more complex bifurcation characteristics. In Case 5 the system bifurcation characteristic changes slightly. Table 5 shows a comparison of Cases 1, 5, and 6 at speed 4251.8 r/min and 7500 r/min.

5.3.2. Calculating Case 1 at Speeds 7320 r/min and 5862 r/min. At speed 7320 r/min, the rotation frequency of sun gear is equal to the second- and third-order natural frequencies under the circumstance of nonfloating shown in Tables 3 and 4. At speed 5862 r/min, that happens in a state of floating. At the two speeds, we calculate Case 1 and plot the bifurcation diagrams shown in Figures 31 and 32. Comparing with Figure 9, we can see that the system bifurcation characteristic is affected by the rotation frequency close to the system fundamental natural frequencies, particularly one close to the natural frequencies of floating status. At speed 5862 r/min,

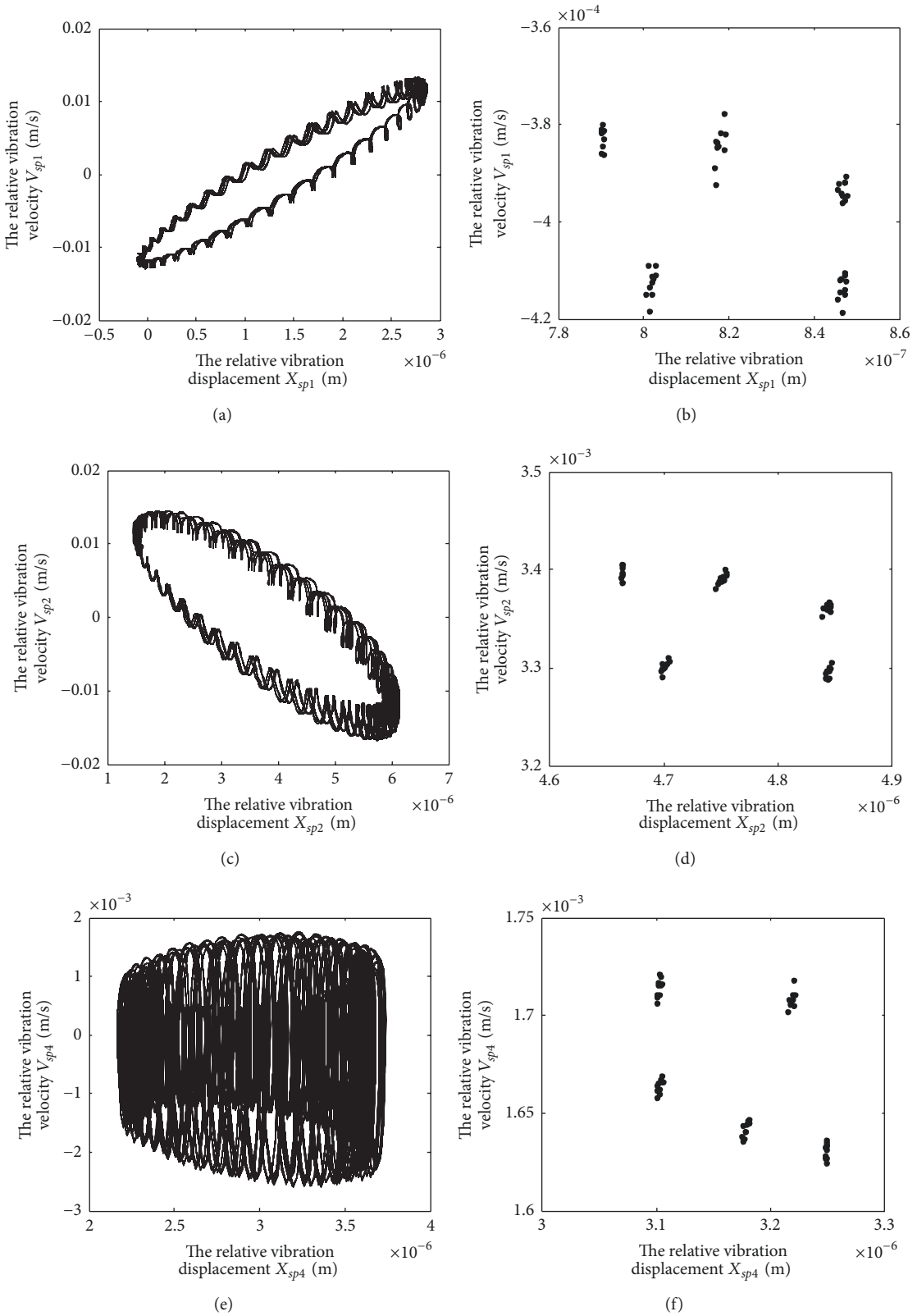

FIGURE 16: The phase plane plots and Poincare maps for five sun-star pairs, when $E_{p1,2,3} = 15\,\mu$m. (a), (c), and (e) are the phase plane plots. (b), (d), and (f) are the Poincare maps (note: only one of the gear pairs which have the same dynamic characteristics is shown).

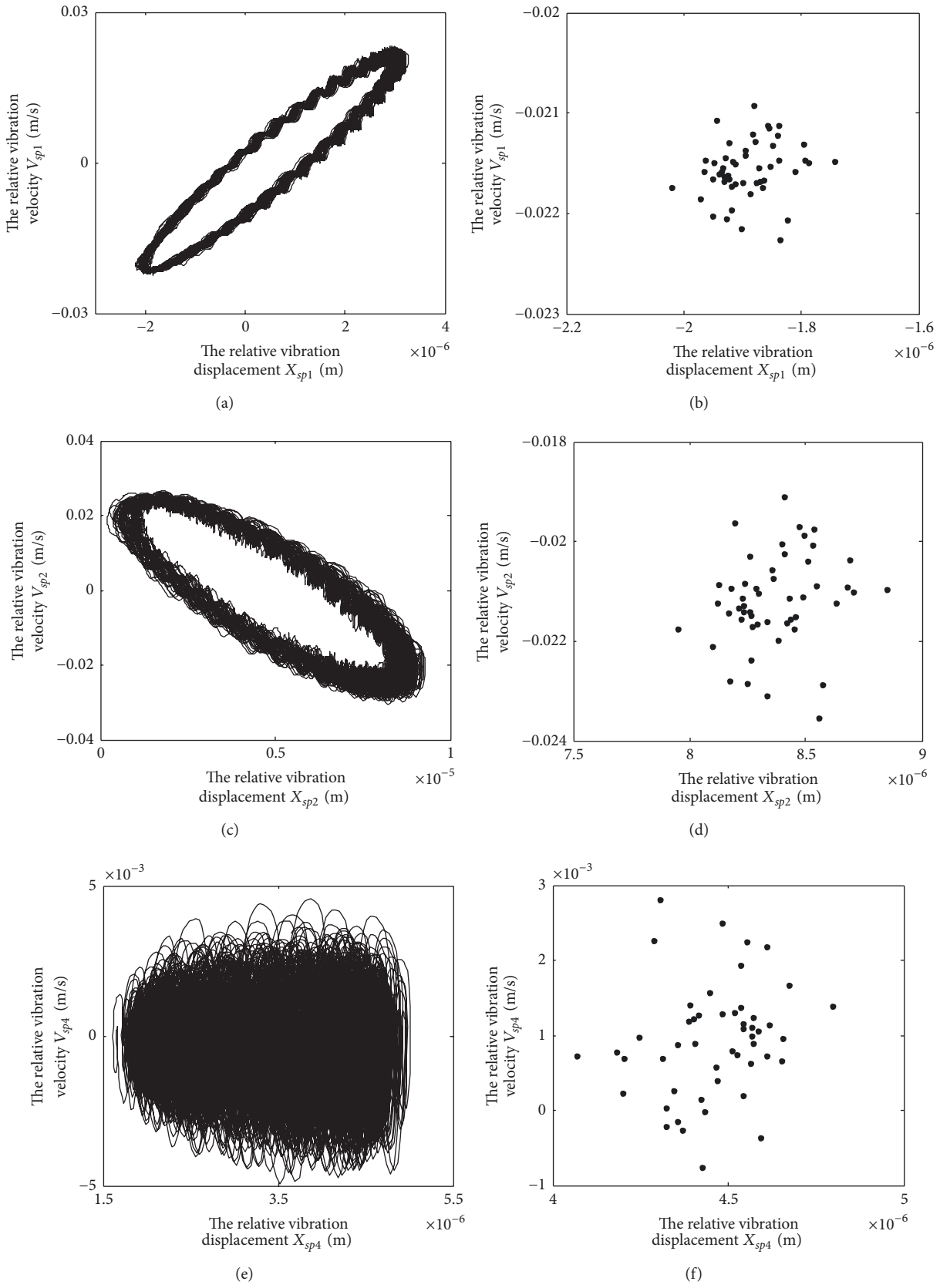

FIGURE 17: The phase plane plots and Poincare maps for five sun-star pairs, when $E_{p1,2,3} = 26.5\,\mu$m. (a), (c), and (e) are the phase plane plots. (b), (d), and (f) are the Poincare maps (note: only one of the gear pairs which have the same dynamic characteristics is shown).

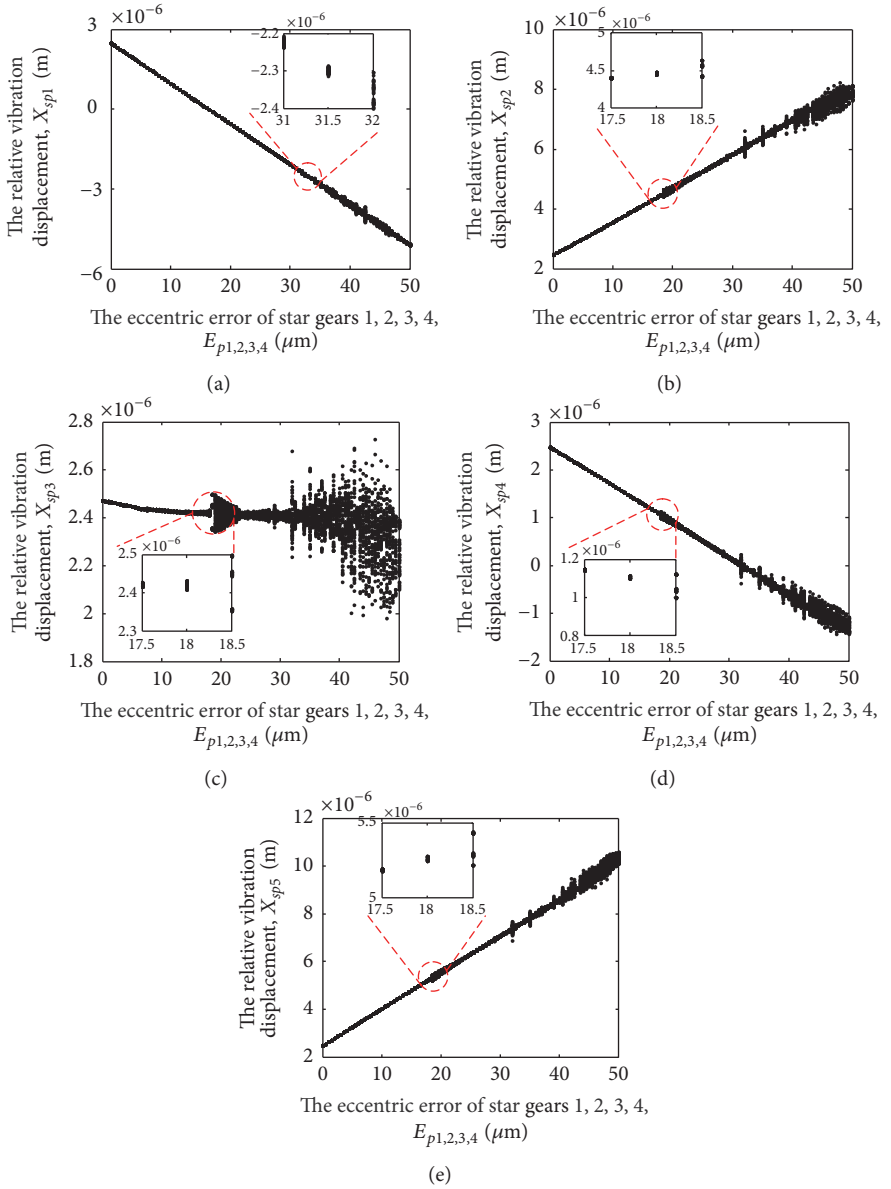

Figure 18: The system bifurcation diagram with the variation of eccentric error of star gears 1, 2, 3, and 4.

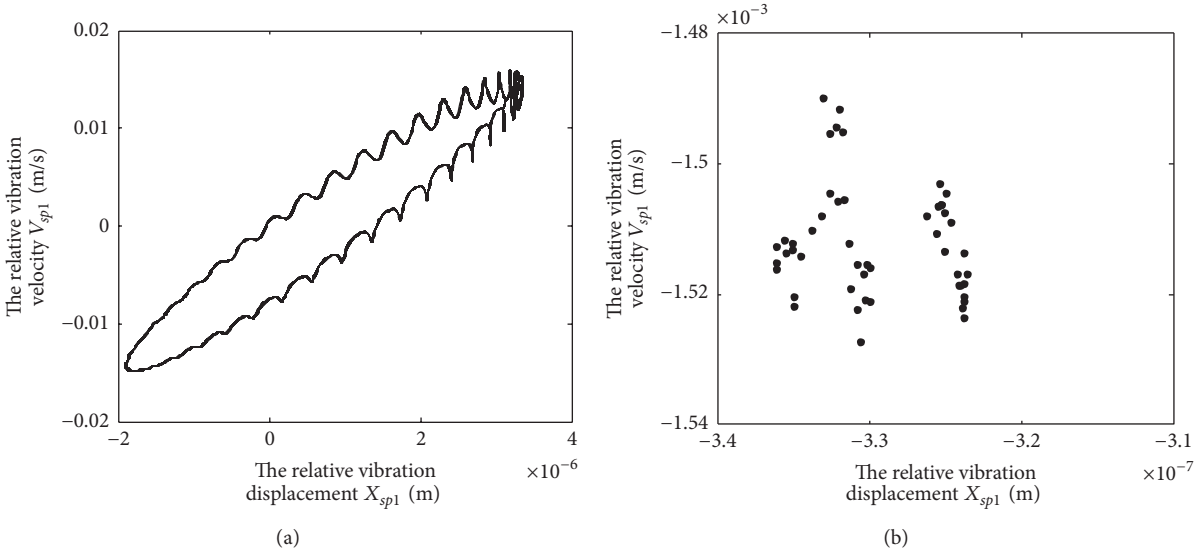

Figure 19: Continued.

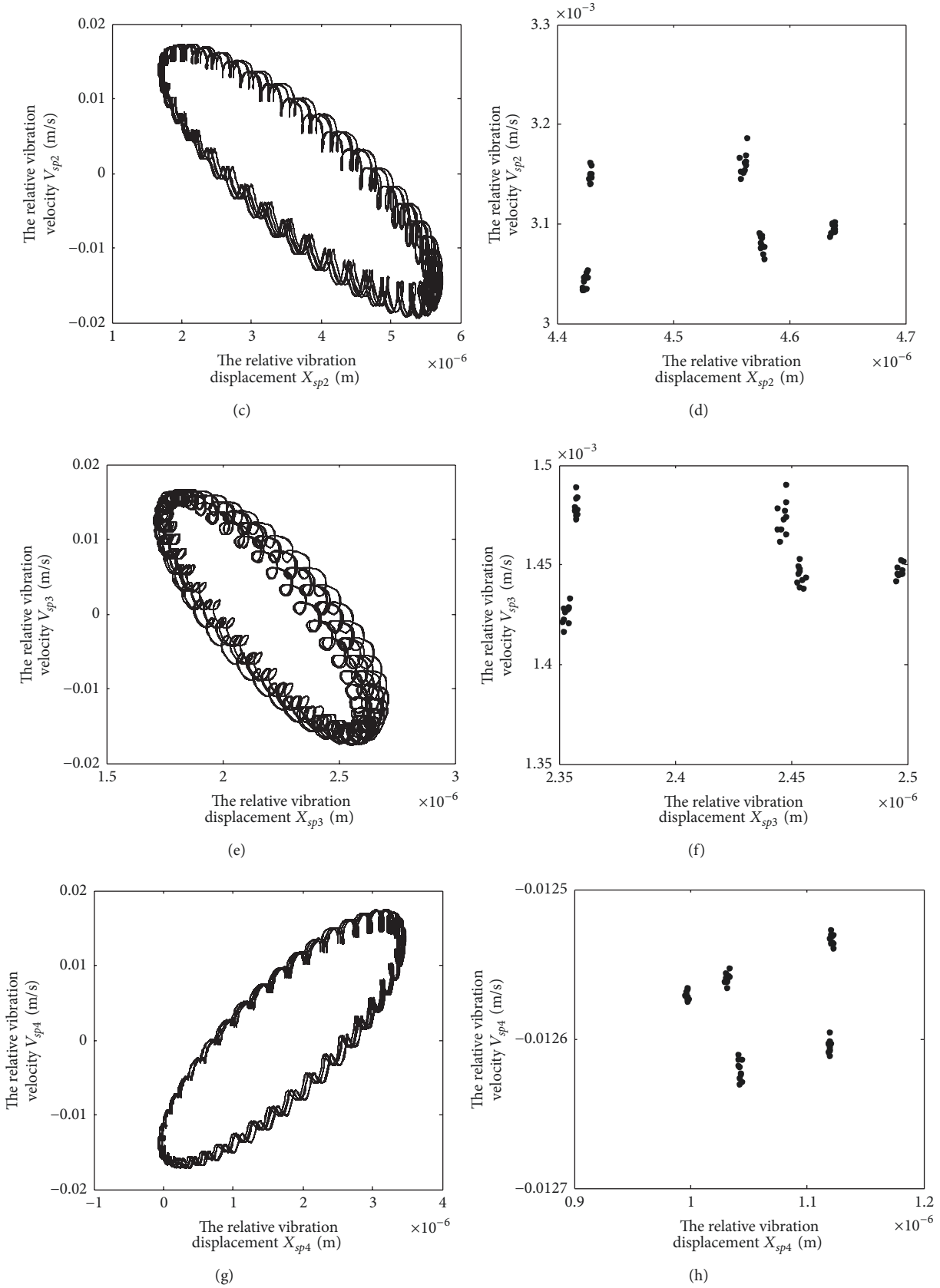

Figure 19: Continued.

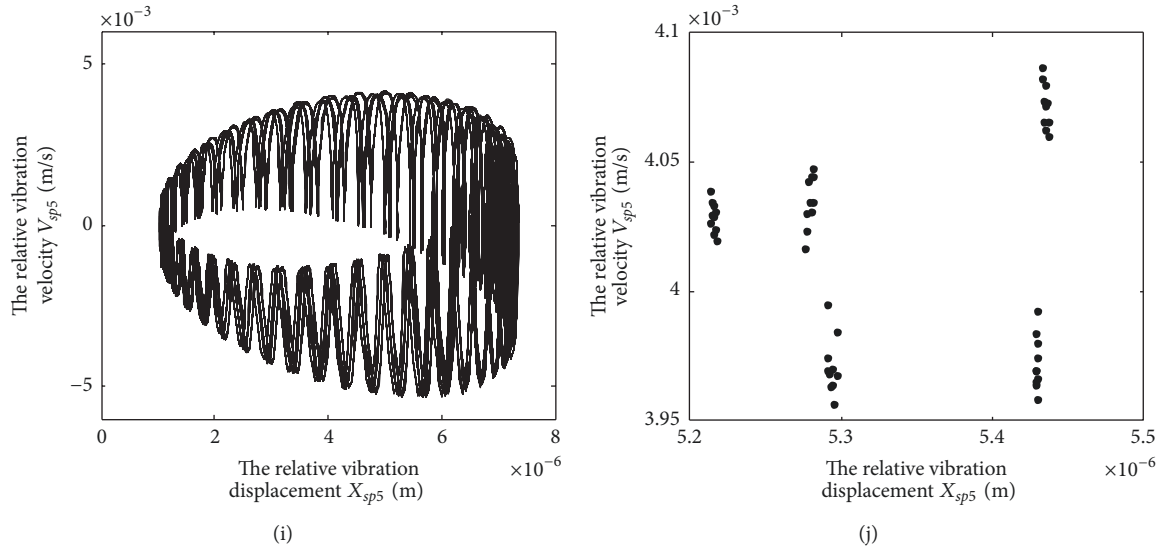

FIGURE 19: The phase plane plots and Poincare maps for five sun-star pairs, when $E_{p1,2,3,4} = 18.5\,\mu$m. (a), (c), (e), (g), and (i) are the phase plane plots. (b), (d), (f), (h), and (j) are the Poincare maps.

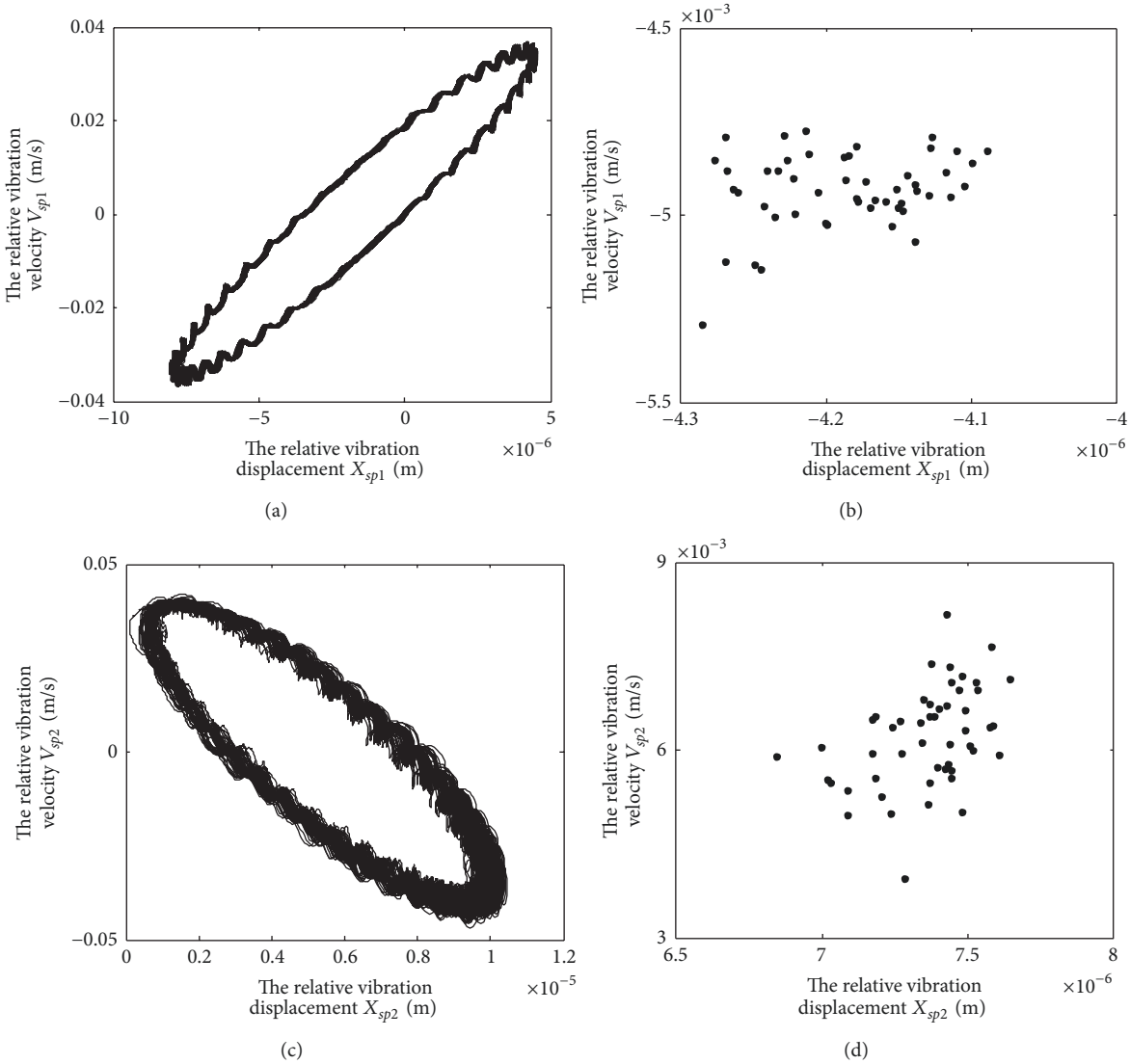

FIGURE 20: Continued.

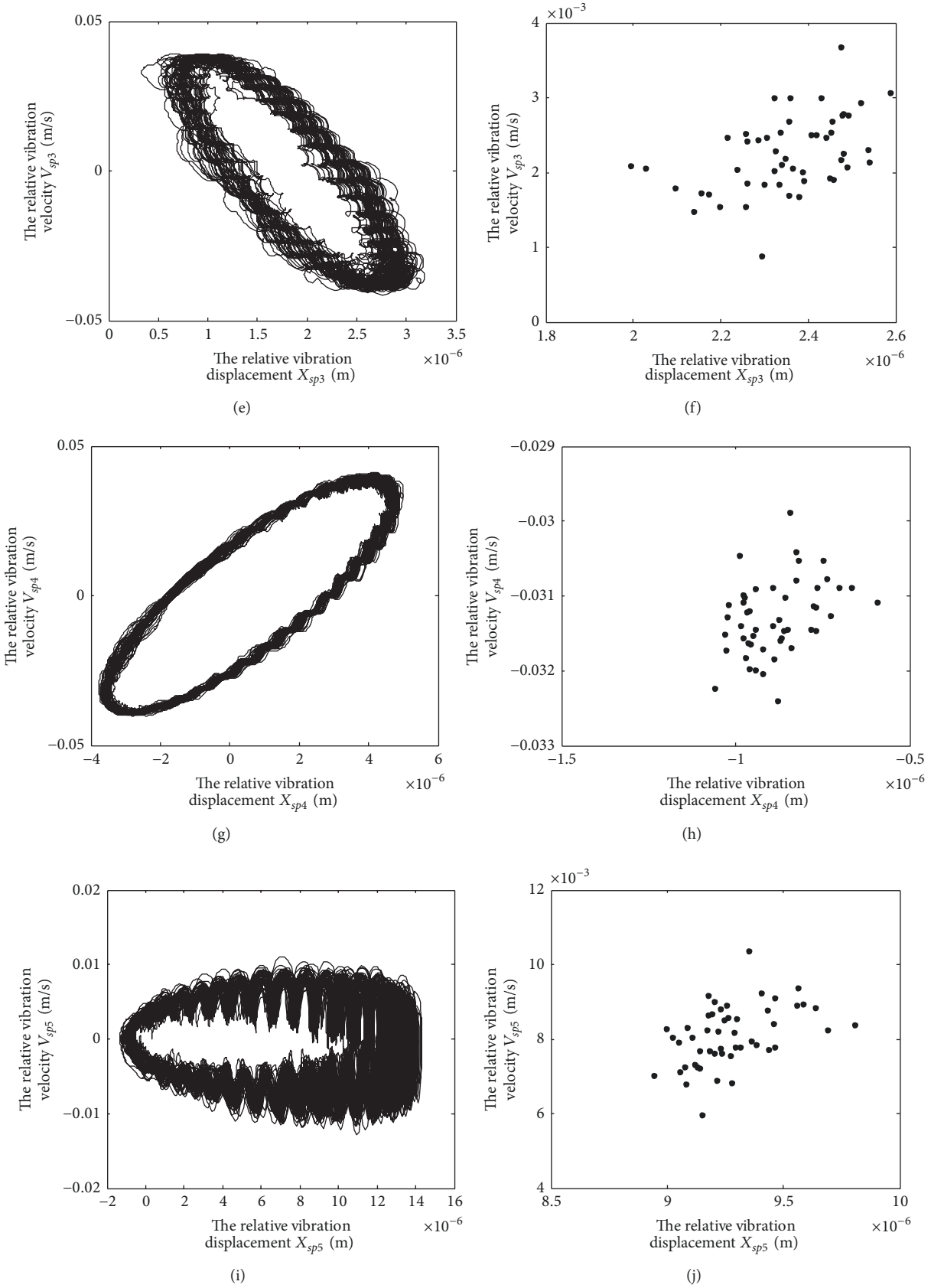

FIGURE 20: The phase plane plots and Poincare maps for five sun-star pairs, when $E_{p1,2,3,4} = 44\,\mu$m. (a), (c), (e), (g), and (i) are the phase plane plots. (b), (d), (f), (h), and (j) are the Poincare maps.

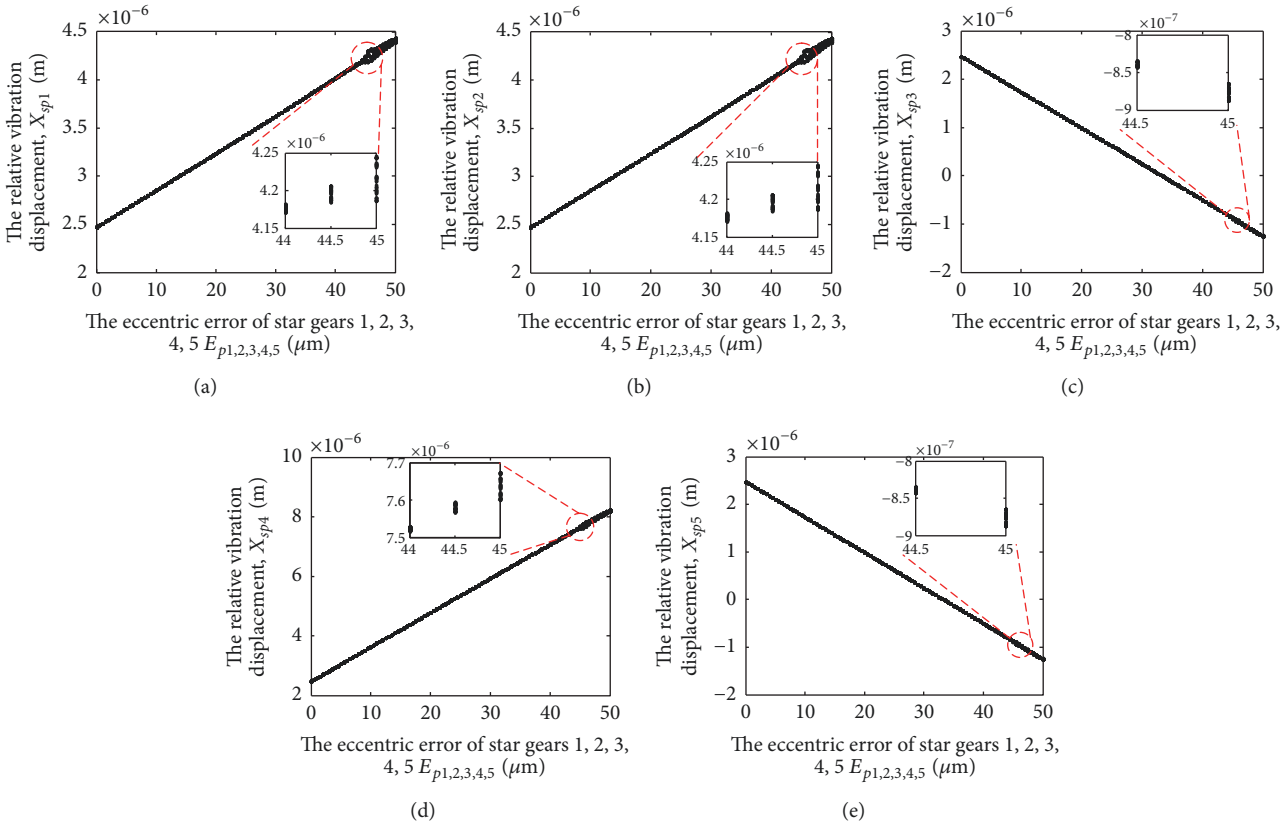

Figure 21: The system bifurcation diagram with the variation of eccentric errors of star gears 1, 2, 3, 4, and 5.

the error values of beginning to bifurcate and showing complex bifurcation characteristics both decrease obviously.

6. Conclusions

This paper mainly analyzes the influence of the variation of eccentric error and working frequencies on the dynamic response of HSGT with floating sun gear. A new and generalized dynamic model for HSGT with floating sun gear is established and solved by Runge-Kutta numerical calculation method. On the basis of the different location and number of star gears, seven cases about eccentric errors are calculated, respectively. Three kinds of working speed are chose to observe the effect of the working frequencies, at which the meshing frequency or rotation frequency is close to the system fundamental natural frequencies. The results are expressed by the bifurcation diagrams, phase plane plots, and Poincare maps. In every case, the system dynamic properties are explained in detail. The main conclusions are summarized as follows:

(1) In any case, the system motion is not always single-period status with the changing of the eccentric errors of star gears. The period-doubling, quasiperiod or chaos motion will happen in the system. Furthermore, the values of the eccentric errors are different when the bifurcations happen in different cases. To compare the bifurcation diagrams, it can be see that the system response of Case 5 is most stale, followed by Cases 6 and 7; the stability of the system response in Cases 2 and 3 is the worst one.

(2) In the premise of the same number of star gears with the eccentric errors, the system response in the case of nonadjacent star gears is more stable than one in the condition of adjacent star gears. This conclusion can be drawn by comparing Cases 2 and 6 as well as Cases 3 and 7.

(3) When the working frequencies (including rotation frequency and meshing frequency) are close to the fundamental natural frequencies the system stability is affected; particularly the effect of meshing frequency is biggest. So in the actual engineering it should be ensured that the working frequencies stay away from every order natural frequency.

The above analysis and conclusions can serve as a guide to the manufacture and assembly in a project of the herringbone star gear transmission with floating sun gear. If the machine accuracy is low, it is necessary to take into account the displacement and number of star gears with eccentric errors in the process of the engineering. In addition, the system working speed should be selected reasonably in case the working frequencies approximate the system fundamental natural frequencies.

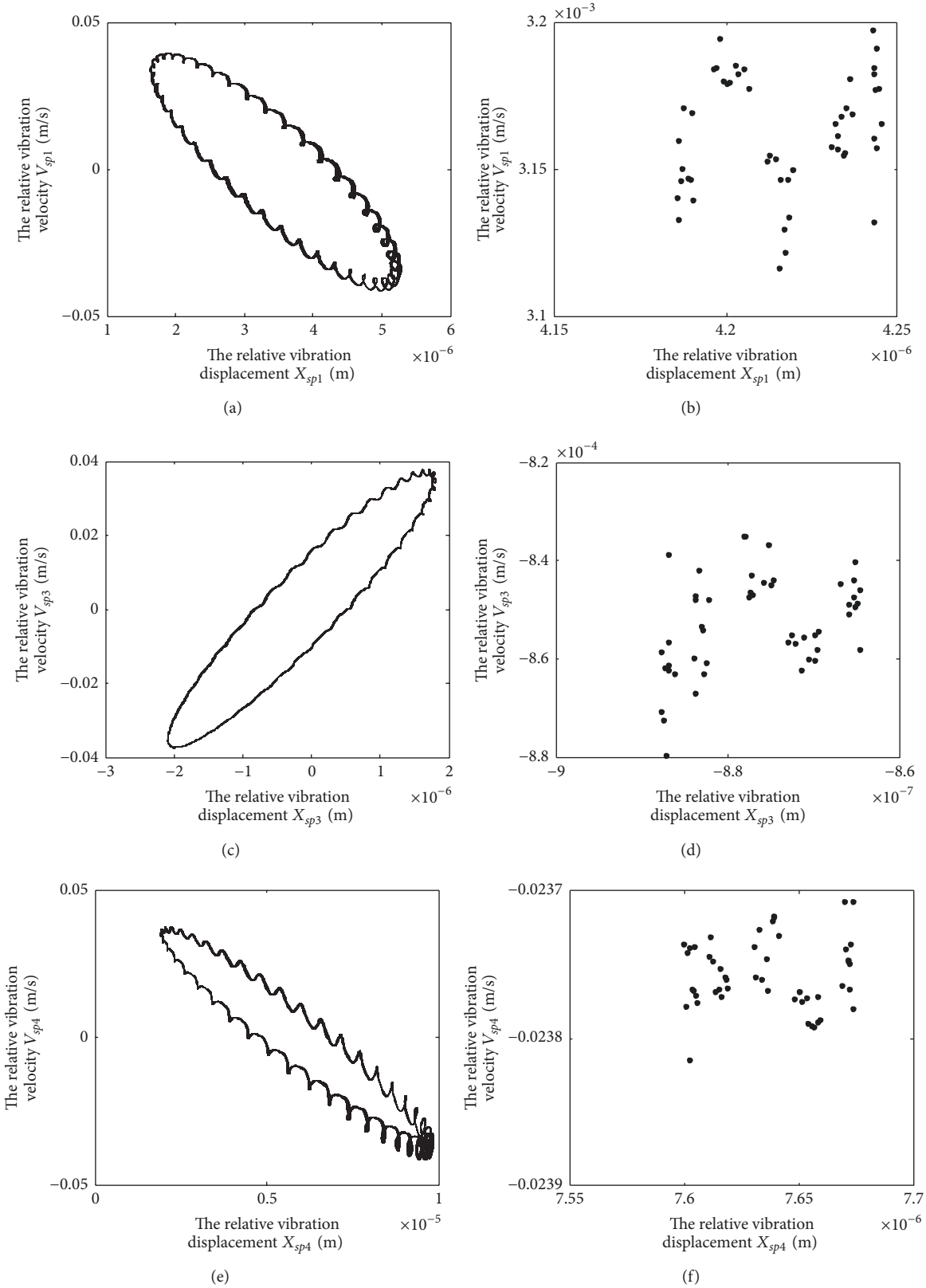

FIGURE 22: The phase plane plots and Poincare maps for five sun-star pairs, when $E_{p1,2,3,4,5} = 45\,\mu$m. (a), (c), and (e) are the phase plane plots. (b), (d), and (f) are the Poincare maps (note: only one of the gear pairs which have the same dynamic characteristics is shown).

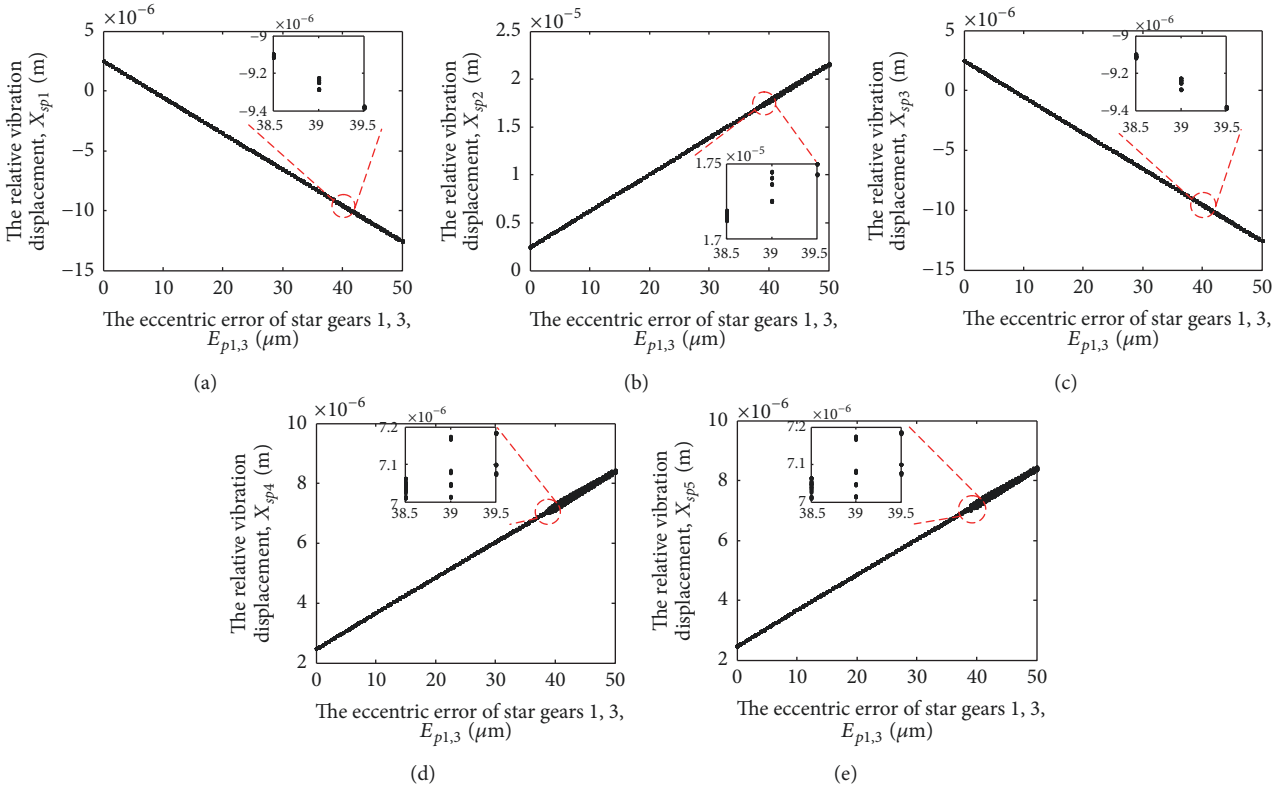

FIGURE 23: The system bifurcation diagram with the variation of eccentric errors of star gears 1 and 3.

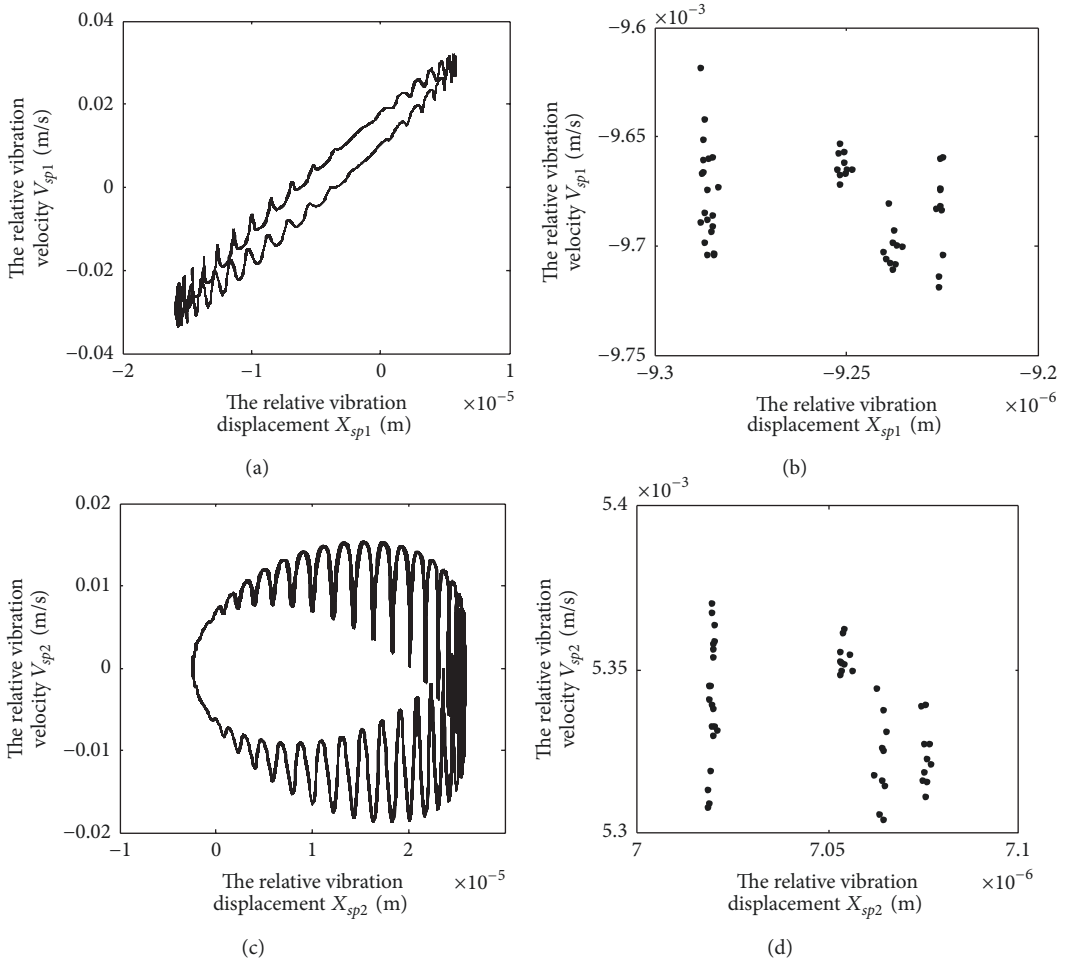

FIGURE 24: Continued.

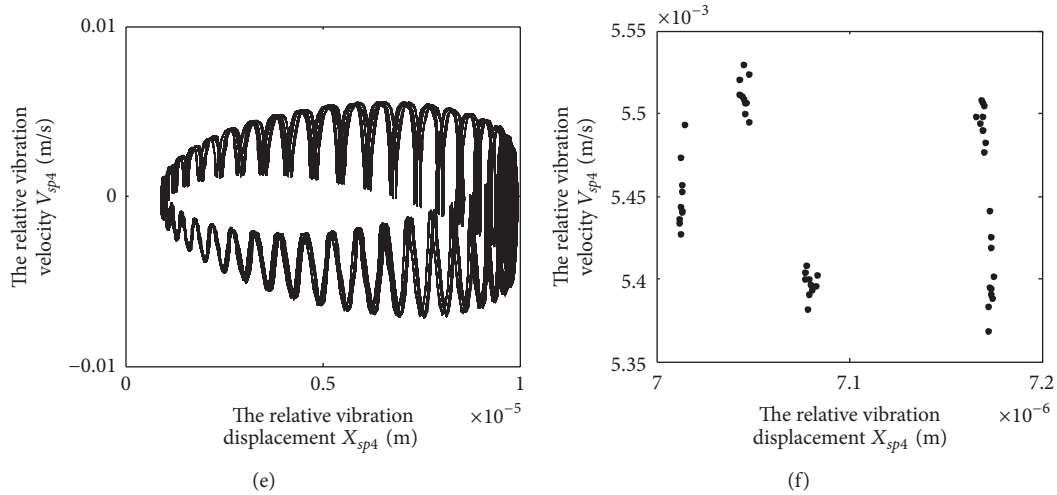

FIGURE 24: The phase plane plots and Poincare maps for five sun-star pairs, when $E_{p1,3} = 39\,\mu$m. (a), (c), and (e) are the phase plane plots. (b), (d), and (f) are the Poincare maps (note: only one of the gear pairs which have the same dynamic characteristics is shown).

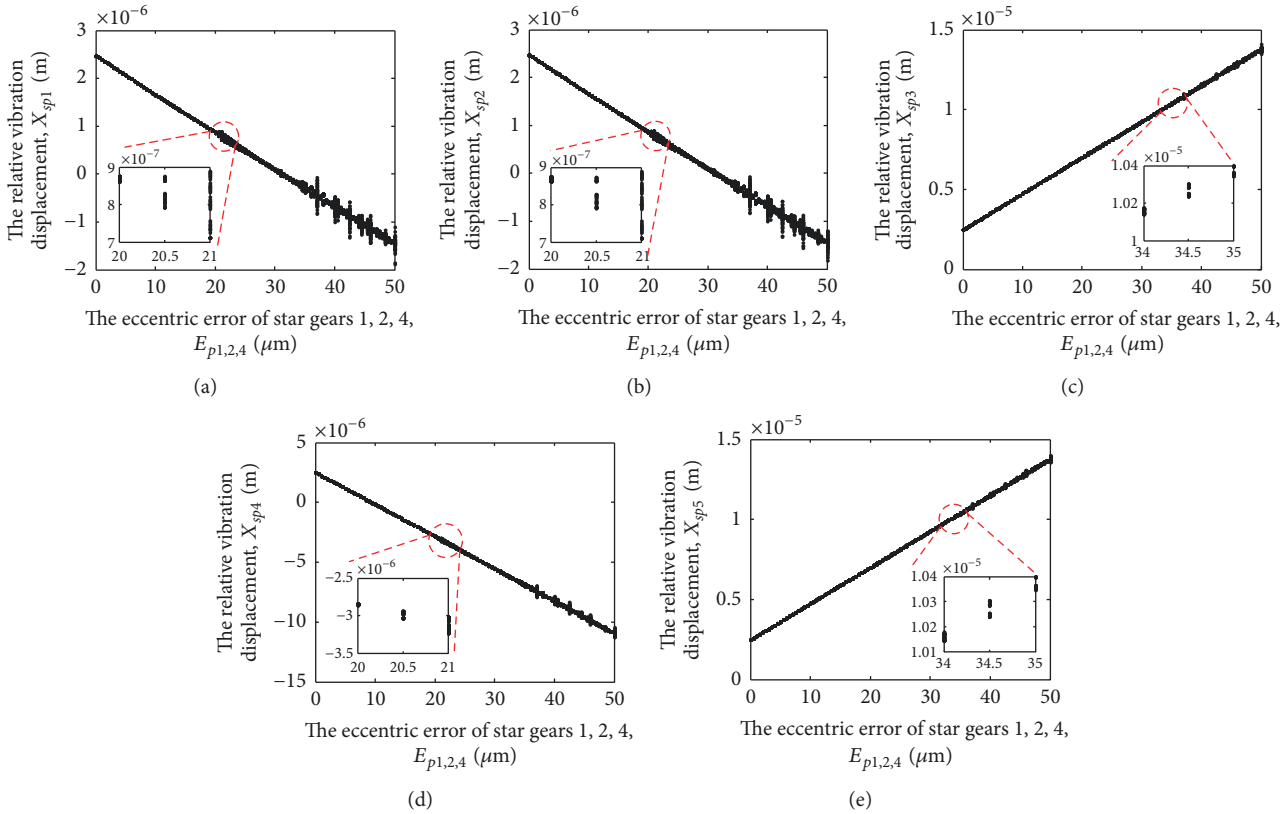

FIGURE 25: The system bifurcation diagram with the variation of eccentric errors of star gears 1 and 2, 4.

Nomenclature

B: The angle between the end meshing line and *x*-axis
C: Damping
E: Eccentric error
e: The equivalent displacements of the eccentric error
F: Force
I: Inertia
K: Stiffness
L: The radial clearance

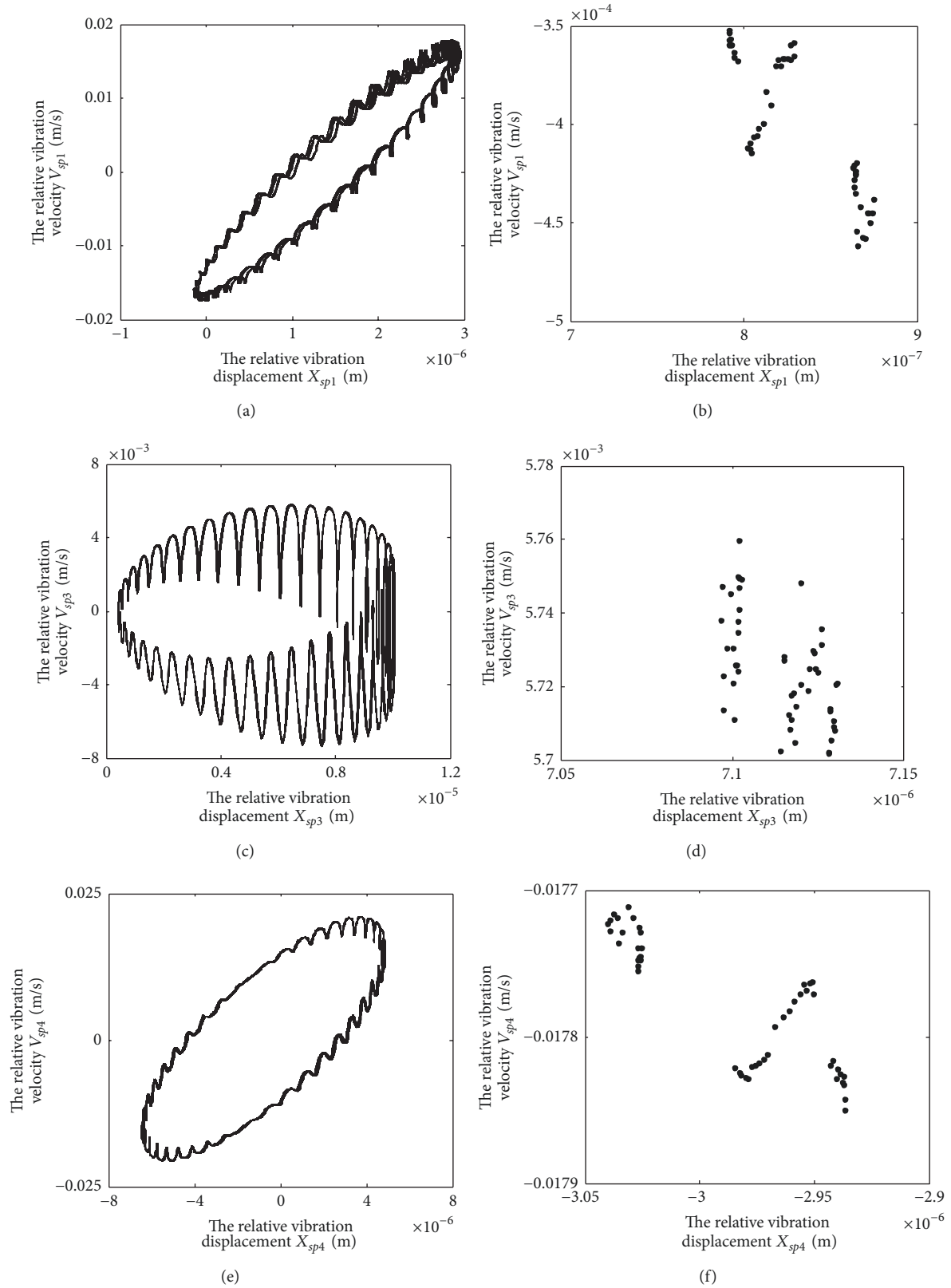

FIGURE 26: The phase plane plots and Poincare maps for five sun-star pairs, when $E_{p1,2,4} = 20.5\,\mu$m. (a), (c), and (e) are the phase plane plots. (b), (d), and (f) are the Poincare maps (note: only one of the gear pairs which have the same dynamic characteristics is shown).

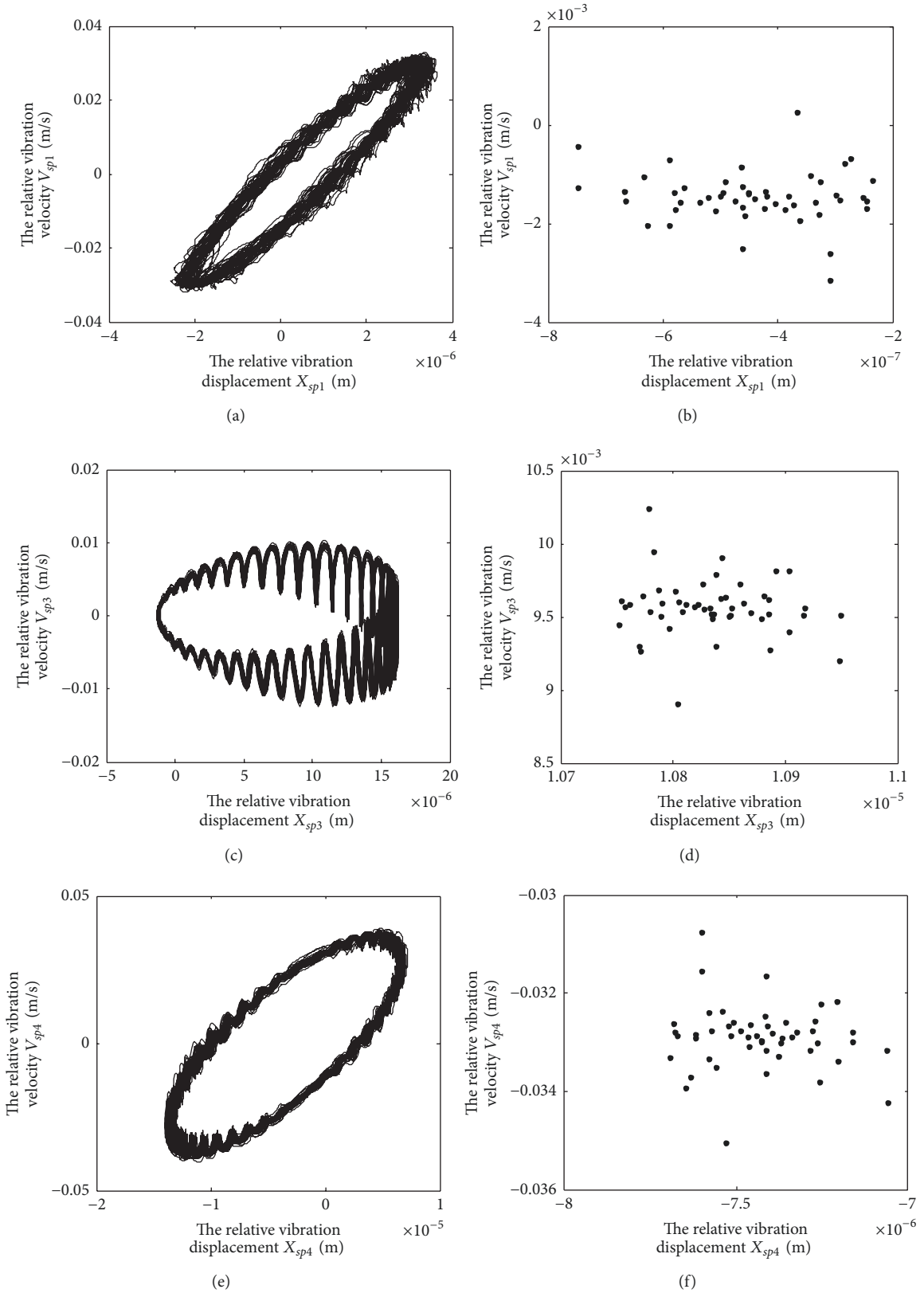

FIGURE 27: The phase plane plots and Poincare maps for five sun-star pairs, when $E_{p1,2,4} = 37\,\mu$m. (a), (c), and (e) are the phase plane plots. (b), (d), and (f) are the Poincare maps (note: only one of the gear pairs which have the same dynamic characteristics is shown).

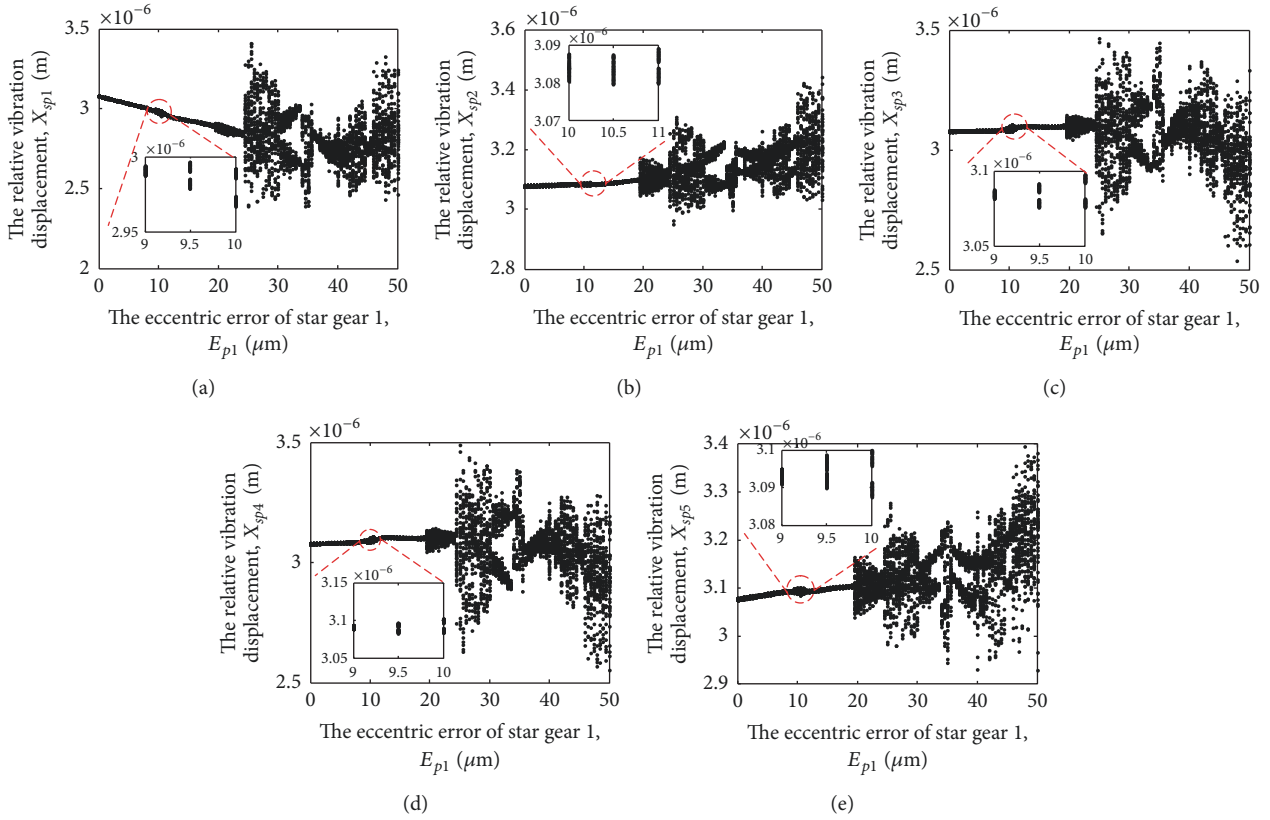

FIGURE 28: The system bifurcation diagram of Case 1 at speed 4251.8 r/min.

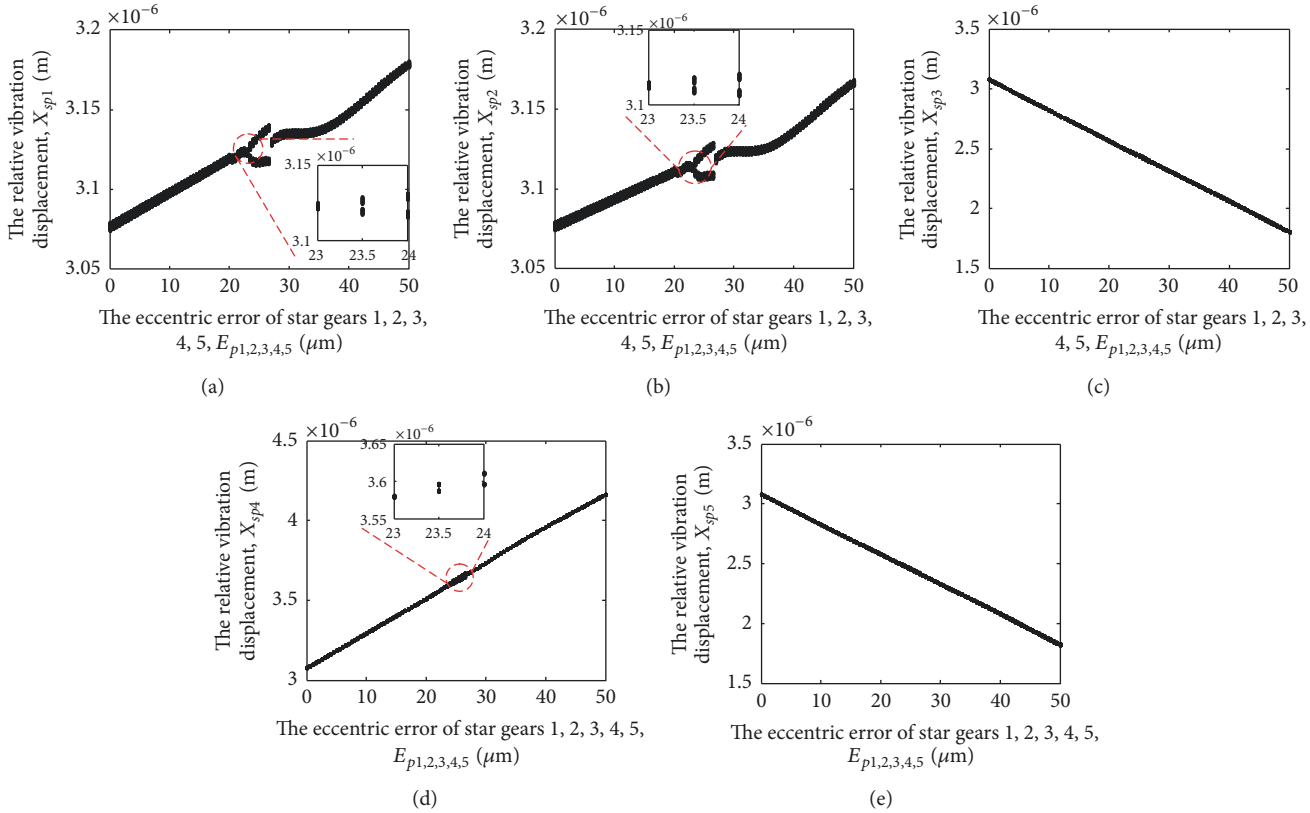

FIGURE 29: The system bifurcation diagram of Case 5 at speed 4251.8 r/min.

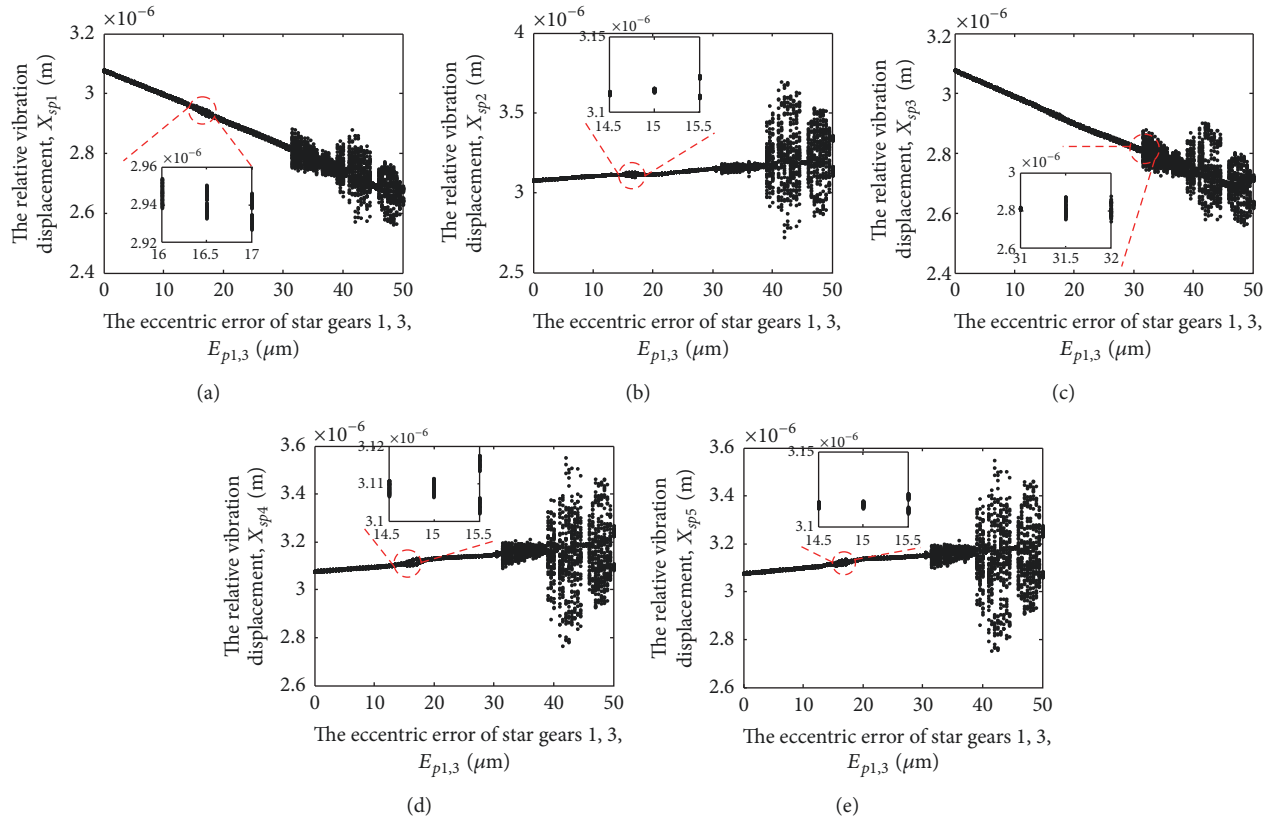

FIGURE 30: The system bifurcation diagram of Case 6 at speed 4251.8 r/min.

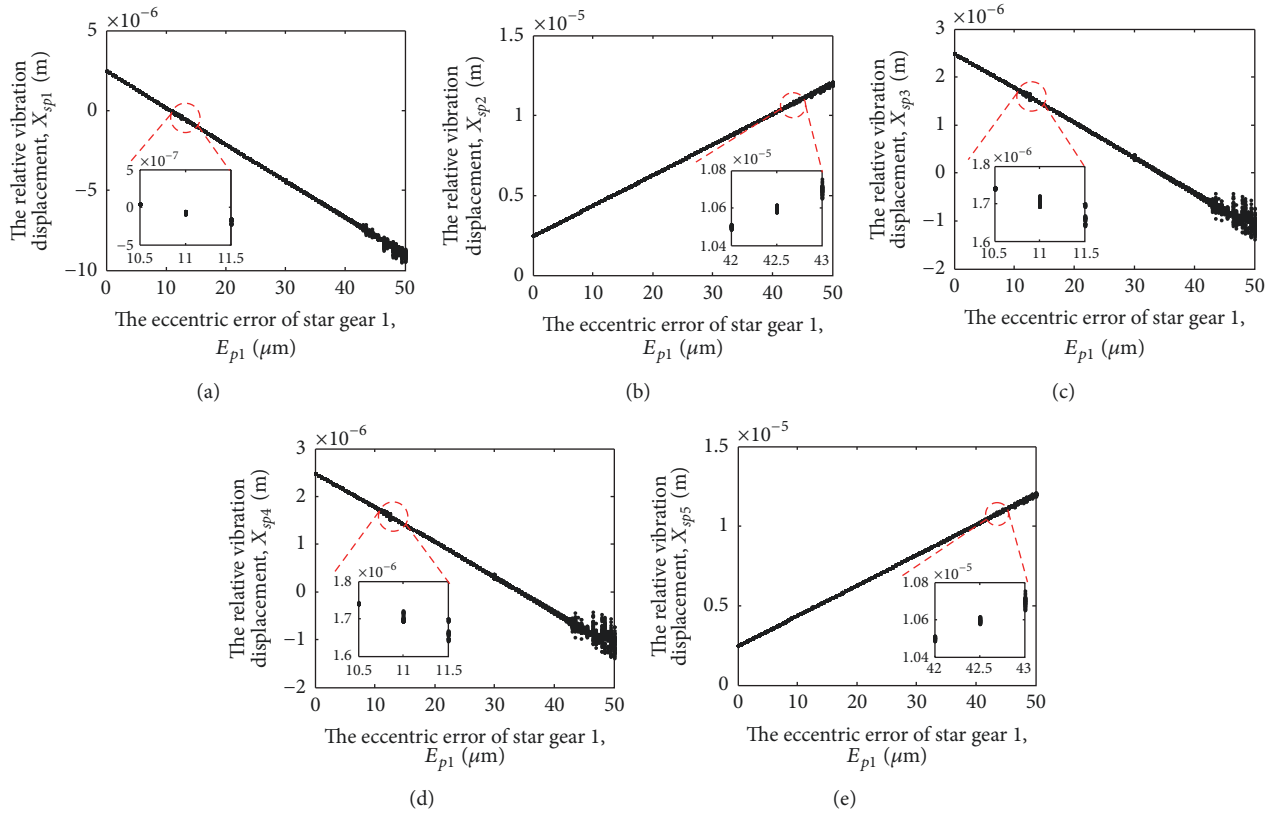

FIGURE 31: The system bifurcation diagram of Case 1 at speed 7320 r/min.

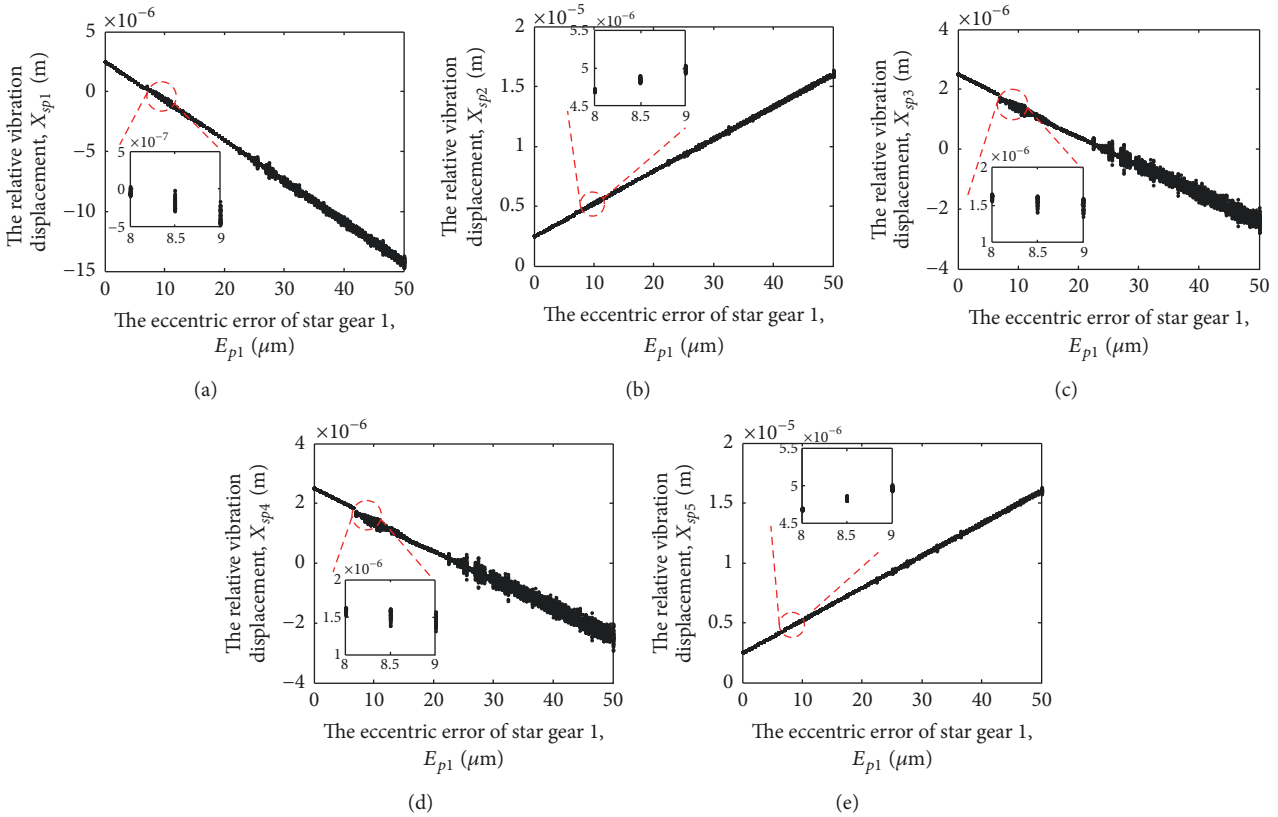

FIGURE 32: The system bifurcation diagram of Case 1 at speed 5862 r/min.

M:	Mass
N:	The number of star gears
$P_{sx/y}$:	The support reaction force of the spline shaft
r:	Base radii
T:	Torque
u:	Rotational displacement
x, y:	Translational displacement
$\alpha_{w/n}$:	The pressure angle of external and inner gearing
β:	The helix angle
γ:	The initial phase of the eccentric error
ω_s, ω_p, ω_r:	The angular velocity
φ:	The assembly position angle of star
Φ:	The angle between the eccentric error and the end meshing line
ξ_t:	The support damping ratio
ξ:	The mesh damping ratio
δ_{spi}, δ_{pir}, $\delta_{picx/y}$:	The relative displacement.

Subscript

b:	Base circle
c:	Carrier
in:	Input
n:	Inner
out:	Output
p:	Star
r:	Ring
s:	Sun
t:	Tangential direct
w:	External.

Conflicts of Interest

The authors declare that they have no conflicts of interest.

Acknowledgments

This work was supported by the National Science Foundation of China (Grant no. 51375384) and the Aeronautical Science Foundation of China (Grant no. 2015ZB55002).

References

[1] S. Mo, Y. Zhang, Q. Wu, H. Houjoh, and S. Matsumura, "Research on natural characteristics of double-helical star gearing system for GTF aero-engine," *Mechanism and Machine Theory*, vol. 106, pp. 166–189, 2016.

[2] T. Hidaka, Y. Terauchi, and K. Dohi, "On the relation between the run-out errors and the motion of the center of sun gear in a stoeckicht planetary gear," *Bulletin of the JSME*, vol. 22, no. 167, pp. 748–754, 1979.

[3] P. Ma and M. Botman, "Load sharing in a planetary gear stage in the presence of gear errors and misalignment," *Journal of Mechanisms, Transmissions, and Automation in Design*, vol. 107, no. 1, pp. 4–10, 1985.

[4] J. Li and L. Wang, "The present status and development of domestic reducer based on the split power technology," *Journal of Mechanical Transmission*, vol. 31, no. 4, pp. 106–110, 2007.

[5] R. August and R. Kasuba, "Torsional vibrations and dynamic loads in a basic planetary gear system," *Journal of Vibration, Acoustics, Stress, and Reliability in Design*, vol. 108, no. 3, pp. 348–353, 1986.

[6] J. Lin and R. G. Parker, "Sensitivity of planetary gear natural frequencies and vibration modes to model parameters," *Journal of Sound and Vibration*, vol. 228, no. 1, pp. 109–128, 1999.

[7] T. Eritenel and R. G. Parker, "Modal properties of three-dimensional helical planetary gears," *Journal of Sound and Vibration*, vol. 325, no. 1-2, pp. 397–420, 2009.

[8] Y. Guo and R. G. Parker, "Dynamic modeling and analysis of a spur planetary gear involving tooth wedging and bearing clearance nonlinearity," *European Journal of Mechanics - A/Solids*, vol. 29, no. 6, pp. 1022–1033, 2010.

[9] C.-J. Bahk and R. G. Parker, "Analytical investigation of tooth profile modification effects on planetary gear dynamics," *Mechanism and Machine Theory*, vol. 70, pp. 298–319, 2013.

[10] T. Sun and H.-Y. Hu, "Nonlinear dynamics of a planetary gear system with multiple clearances," *Mechanism and Machine Theory*, vol. 38, no. 12, pp. 1371–1390, 2003.

[11] H. Ligata, A. Kahraman, and A. Singh, "An experimental study of the influence of manufacturing errors on the planetary gear stresses and planet load sharing," *Journal of Mechanical Design*, vol. 130, no. 4, Article ID 041701, 2008.

[12] M. Iglesias, A. Fernández, A. de Juan, A. Díez, P. García, and F. Viadero, "Planet eccentricity error on a planetary gear transmission: influence on load sharing," in *Proceedings of the 9th IFToMM International Conference on Rotor Dynamics*, P. Pennacchi, Ed., 21, pp. 1381–1390, Rome, Italy, 2015.

[13] R. G. Parker, V. Agashe, and S. M. Vijayakar, "Dynamic response of a planetary gear system using a finite element/contact mechanics model," *Journal of Mechanical Design*, vol. 122, no. 3, pp. 304–310, 2000.

[14] R. G. Parker, "Physical explanation for the effectiveness of planet phasing to suppress planetary gear vibration," *Journal of Sound and Vibration*, vol. 236, no. 4, pp. 561–573, 2000.

[15] J. Lin and R. G. Parker, "Planetary gear parametric instability caused by mesh stiffness variation," *Journal of Sound and Vibration*, vol. 249, no. 1, pp. 129–145, 2002.

[16] A. N. Montestruc, "Influence of planet pin stiffness on load sharing in planetary gear drives," *Journal of Mechanical Design*, vol. 133, no. 1, Article ID 014501, 2011.

[17] A. Bodas and A. Kahraman, "Influence of carrier and gear manufacturing errors on the static load sharing behavior of planetary gear sets," *JSME International Journal Series C Mechanical Systems, Machine Elements and Manufacturing*, vol. 47, no. 3, pp. 908–915, 2004.

[18] M. Inalpolat and A. Kahraman, "A dynamic model to predict modulation sidebands of a planetary gear set having manufacturing errors," *Journal of Sound and Vibration*, vol. 329, no. 4, pp. 371–393, 2010.

[19] F. Ren, D. Qin, T. C. Lim, and S. Lyu, "Study on dynamic characteristics and load sharing of a herringbone planetary gear with manufacturing errors," *International Journal of Precision Engineering and Manufacturing*, vol. 15, no. 9, pp. 1925–1934, 2014.

[20] J. Lin and R. G. Parker, "Analytical characterization of the unique properties of planetary gear free vibration," *Journal of Vibration and Acoustics*, vol. 121, no. 3, pp. 316–321, 1999.

[21] A. Kahraman and S. Vijayakar, "Effect of internal gear flexibility on the quasi-static behavior of a planetary gear set," *Journal of Mechanical Design—Transactions of the ASME*, vol. 123, no. 3, pp. 408–415, 2001.

[22] N. Ge and J. Zhang, "Finite element analysis of internal gear in high-speed planetary gear units," *Transactions of Tianjin University*, vol. 14, no. 1, pp. 11–15, 2008.

[23] Z. Sun, Y. Shen, S. Wang, and Y. Hou, "Nonlinear dynamic model and dynamic tooth loads analysis of star gearing system," *Journal of Aerospace Power*, vol. 16, no. 4, pp. 402–407, 2001 (Chinese).

[24] Z. Sun, Y. Shen, S. Wang, and H. Li, "On nonlinear dynamic behavior of star gear system due to clearances," *Xibei Gongye Daxue Xuebao/Journal of Northwestern Polytechnical University*, vol. 20, no. 2, pp. 222–226, 2002.

[25] H. Bao and R. Zhu, "Analysis of dynamic load sharing in a 2-stage planet gear train," *Journal of Aerospace Power*, vol. 6, no. 20, pp. 938–943, 2005.

[26] S. Mo, Y. Zhang, Q. Wu, F. M. Wang, S. Matsumura, and H. Houjoh, "Load sharing behavior of star gearing reducer for geared turbofan engine," *Chinese Journal of Mechanical Engineering*, vol. 30, pp. 1–7, 2017.

[27] F. L. Litvin and A. Fuentes, *Gear Geometry and Applied Theory*, Cambridge University Press, Cambridge, UK, 2004.

[28] Z. Fang, "Model and approach for loaded tooth contact analysis (LTCA) of gear drives," *Mechanical Transmission*, vol. 2, no. 22, pp. 16–52, 1998.

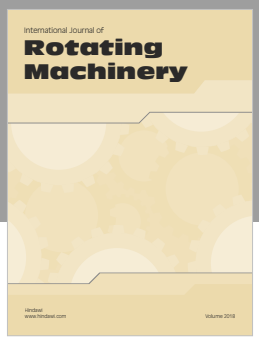

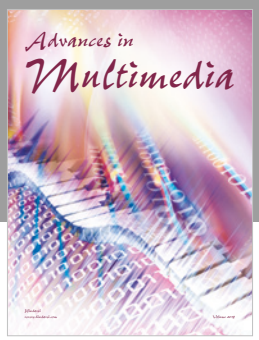

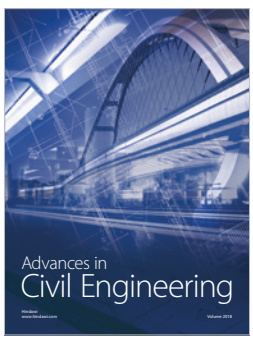

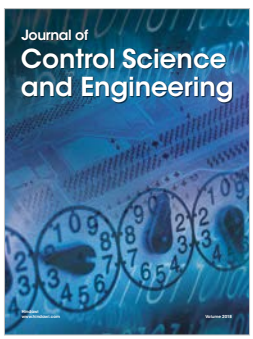

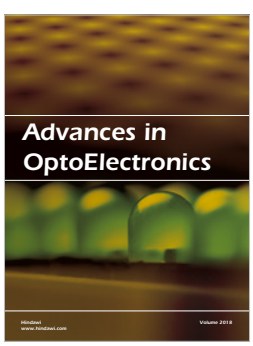

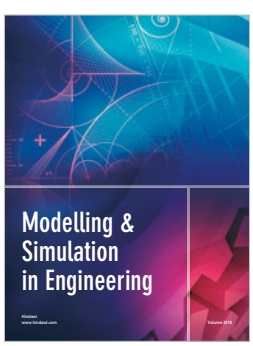

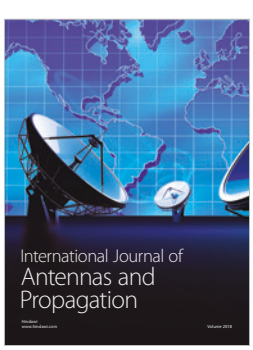

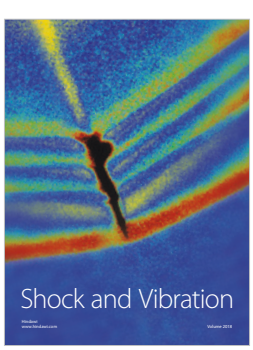

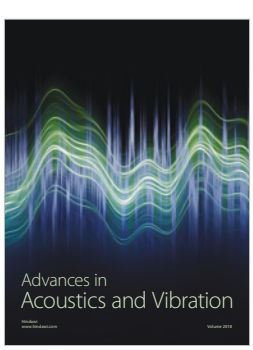

Hindawi

Submit your manuscripts at
www.hindawi.com